THE OHIO STATE UNIVERSITY

Reconfigurable Printed Antenna for GPS Applications

R.G. Rojas, K.W. Lee and N. Surittikul

The Ohio State University

ElectroScience Laboratory

Department of Electrical Engineering
1320 Kinnear Road
Columbus, Ohio 43212

Final Report 739356-2
Agreement No. F49620-00-1-0318
September 2001

U.S. Air Force, AFRL, AF Office of Scientific Research
801 N. Randolph St., Room 732
Arlington, VA 22203-1977

20011126 097

A. Approved for public release; Distribution is unlimited

50272-101

REPORT DOCUMENTATION PAGE	1. REPORT NO.	2. AFRL-SR-BL-TR-01-0563

4. Title and Subtitle

Reconfigurable Printed Antenna for GPS Applications

6.

7. Author(s)

R.G. Rojas, K.W. Lee and N. Surittikul

8. Performing Org. Rept. No.

739356-2

9. Performing Organization Name and Address

The Ohio State University
ElectroScience Laboratory
1320 Kinnear Road
Columbus, OH 43212

10. Project/Task/Work Unit No.

11. Contract(C) or Grant(G) No.

(C)

(G) F49620-00-1-0318

12. Sponsoring Organization Name and Address

U.S. Air Force, AFRL, AF Office of Scientific Research
801 N. Randolph St., Room 732
Arlington, VA 22203-1977

13. Report Type/Period Covered

Final Report

15. Supplementary Notes

AIR FORCE OFFICE OF SCIENTIFIC RESEARCH (AFOSR)
NOTICE OF TRANSMITTAL DTIC. THIS TECHNICAL REPORT
HAS BEEN REVIEWED AND IS APPROVED FOR PUBLIC RELEASE
LAW AFR 190-12. DISTRIBUTION IS UNLIMITED.

16. Abstract (Limit: 200 words)

This final report discusses three issues related to the design of reconfigurable printed antenna for GPS applications. The first one deals with a brief study of four key parameters, namely, ring, ground plane and substrate dimensions as well as substrate thickness. The dependence of the radiation pattern on the dimensions of these parameters is discussed. Surface currents induced on the ring are also calculated to understand the behavior of the ring. We also compare the behavior of this antenna with the well known Yagi-Uda array and briefly present a scheme to reduce the overall size of the parasitic ring. The second topic addressed here deals with improvements made to a computer code based on the Finite Difference Time Domain (FDTD). Although the original code is reasonably accurate, it requires improvements in the calculation of the input impedance for probe-fed microstrip antennas. Another major improvement is needed to compute the radiation pattern of a patch with thin slots. These slots are needed to decrease the overall size of the antenna. The final topic discussed here is an study of the performance of a version of the reconfigurable antenna (there are two designs) in the presence of jamming signals. We also define coverage and calculate this parameter. The antenna is assumed to be mounted on an infinite planar ground plane. This is a rough model for a large cylindrical structure that will be used in the future to model the fuselage of aircraft.

17. Document Analysis a. Descriptors

reconfigurable GPS antenna
FDTD
coverage
microstrip antenna
jamming signals

b. Identifiers/Open-Ended Terms

c. COSATI Field/Group

18. Availability Statement	19. Security Class (This Report)	21. No. of Pages
A. Approved for public release; Distribution is unlimited.	Unclassified	67
	20. Security Class (This Page) Unclassified	22. Price

(See ANSI-Z39.18) *See Instructions on Reverse* **OPTIONAL FORM 272 (4-77)** **Department of Commerce**

Contents

List of Figures iv

1 Introduction 1
- 1.1 Overview . . . 1
- 1.2 Technology Transition . . . 3

2 Circularly Polarized Antenna - Small Ground Plane 5
- 2.1 Parametric Study - Ring Size . . . 6
- 2.2 Parametric Study - Ground Plane Size . . . 7
- 2.3 Parametric Study - Substrate Size . . . 8

3 Surface Current Analysis 19
- 3.1 Analysis of Induced Surface Currents . . . 20
- 3.2 Comparison of Parasitic Ring with Parasitic Elements in Yagi-Uda Array 24
- 3.3 Scheme to Reduce Ring Dimensions . . . 25

4 FDTD Improvements 36
- 4.1 Input Impedance . . . 36
- 4.2 Narrow Slot model . . . 38

5 Antenna Performance in Presence of Jamming signals 46
- 5.1 System Configuration . . . 53
- 5.2 Antenna Performance . . . 57

6 Conclusion 63

Bibliography 66

List of Figures

1.1 Design II : Circularly polarized microstrip antenna with metallic ring around the patch and ground plane 2

2.1 Circularly polarized microstrip antenna with small ground plane and diode-loaded metallic ring around the patch (top view) 6
2.2 Calculated E_{RHCP} antenna pattern at $L1$ in $y-z$ plane of a RHCP antenna ($h = 0.8$ cm) loaded with a metallic ring with size $S_1 \times S_2$. . 9
2.3 Calculated E_{LHCP} antenna pattern at $L1$ in $y-z$ plane of a RHCP antenna ($h = 0.8$ cm) loaded with a metallic ring with size $S_1 \times S_2$. . 10
2.4 Calculated E_{RHCP} antenna pattern at $L1$ in $y-z$ plane of a RHCP antenna ($h = 0.27$ cm) loaded with a metallic ring with size $S_1 \times S_2$. . 11
2.5 Calculated E_{LHCP} antenna pattern at $L1$ in $y-z$ plane of a RHCP antenna ($h = 0.27$ cm) loaded with a metallic ring with size $S_1 \times S_2$. . 12
2.6 Calculated E_{RHCP} antenna pattern at $L1$ in $y-z$ plane of a RHCP antenna ($h = 0.13$ cm) loaded with a metallic ring with size $S_1 \times S_2$. . 13
2.7 Calculated E_{LHCP} antenna pattern at $L1$ in $y-z$ plane of a RHCP antenna ($h = 0.13$ cm) loaded with a metallic ring with size $S_1 \times S_2$. . 14
2.8 Calculated E_{RHCP} antenna pattern at $L1$ in $y-z$ plane of a RHCP antenna loaded with a metallic ring with different ground plane dimensions $L_3 \times L_4$. 15
2.9 Calculated E_{LHCP} antenna pattern at $L1$ in $y-z$ plane of a RHCP antenna loaded with a metallic ring with different ground plane dimensions $L_3 \times L_4$. 16
2.10 Calculated E_{RHCP} antenna pattern at $L1$ in $y-z$ plane of a RHCP antenna loaded with a metallic ring with different substrate dimensions $L_1 \times L_2$. 17
2.11 Calculated E_{LHCP} antenna pattern at $L1$ in $y-z$ plane of a RHCP antenna loaded with a metallic ring with different substrate dimensions $L_1 \times L_2$. 18

3.1 Induced surface current model. (a) Original ring structure. (b) Induced surface currents. 19
3.2 Calculated E_{RHCP} antenna pattern at $L1$ in (a) $y-z$ plane and (b) $x-z$ plane of a RHCP antenna loaded with a pair of metallic strips in $x-$ direction. 21

3.3 Calculated E_{RHCP} antenna pattern at $L1$ in (a) $y-z$ plane and (b) $x-z$ plane of a RHCP antenna loaded with a pair of metallic strips in $y-$ direction. 22
3.4 Calculated (a) E_ϕ and (b) E_θ antenna pattern at $L1$ of a RHCP antenna loaded with a pair of metallic strips in $x-$ direction as shown in Fig. 3.2. 26
3.5 Induced surface current J_{sy} (left) and J_{sx} (right). 27
3.6 Induced surface current J_{sy} (left) and J_{sx} (right) (a smaller amplitude scale to show the strip current amplitudes). 28
3.7 Induced surface current J_{sy} (left) and J_{sx} (right) along a metallic strip. 29
3.8 Induced surface current J_{sy} of the metallic ring with $h = 0.8$ cm and for different ring dimensions. 30
3.9 Induced surface current J_{sx} of the metallic ring with $h = 0.8$ cm and different ring dimensions. 31
3.10 Induced surface current J_{sx} of the metallic ring with $h = 0.27$ cm and different ring dimensions. 32
3.11 Yagi-Uda array configuration. 33
3.12 Calculated E_{RHCP} pattern of the reconfigurable antenna with capacitive loading. 34
3.13 Calculated E_{RHCP} pattern of the reconfigurable antenna with inductive loading. 35

4.1 Faraday's law contour path for the thin wire FDTD modification . . 37
4.2 Input impedance comparison between FDTD computation and measured result of microstrip antenna 39
4.3 Input impedance comparison between modified FDTD code and measured result of microstrip antenna 40
4.4 Faraday's law contour paths for 12 different two-dimensional planar conducting screen cases 42
4.5 Faraday's law contour paths for 10 different two-dimensional planar conducting screen cases where the slot width is smaller than the grid size 43
4.6 E-plane field patterns of a single-feed circularly polarized microstrip antenna with a slit 44
4.7 H-plane field patterns of a single-feed circularly polarized microstrip antenna with a slit 45

5.1 Design I: Circularly polarized microstrip antenna with an array of diode-loaded metallic strips (top view). Note that ground plane is larger than the ring. In this case the ground plane is the same size as the substrate 47
5.2 Circularly polarized microstrip antenna without a metallic ring (top view) 48
5.3 Circularly polarized microstrip antenna with one metallic ring (diode on) 49

5.4 Circularly polarized microstrip antenna with two metallic rings (diode off) 50
5.5 Antenna mounted on convex surface 51
5.6 Reconfigurable antenna mounted on planar ground plane (top view). Jamming signals can be incident from any direction in azimuth . . . 52
5.7 Radiation patterns of reconfigurable antenna in $0^o, 30^o$ and 60^o plane cuts, L1 band 54
5.8 Radiation patterns of reconfigurable antenna in $90^o, 120^o$ and 150^o plane cuts, L1 band 55
5.9 An scenario for reconfigurable antenna performance test (side view) . 56
5.10 Received jamming power as a function of number of jammers 59
5.11 Interference suppression of the reconfigurable antenna with respect to ideal isotropic antenna 60
5.12 Interference suppression of reconfigurable antenna with respect to case when all switches in parasitic ring are turned on 61
5.13 GPS antenna coverage as a function of antenna gain $\tilde{G}$ 62

Acknowledgment

This material is based on research sponsored by the Air Force Research Laboratory, under agreement number F49620-00-1-0318. The U.S. Government is authorized to reproduce and distribute reprints for Governmental purposes notwithstanding any copyright notation thereon.

The views and conclusions contained herein are those of the authors and should not be interpreted as necessarily representing the official policies or endorsements, either expressed or implied, of the Air Force Research Laboratory or the U.S. government

Chapter 1

Introduction

1.1 Overview

The widespread use of satellite communication systems such as the Global Positioning System (GPS) in navigation, surveying and other applications requires high performance receivers and antennas, especially in terms of precision and reliability [1]. In the design of high performance GPS receiving antennas, several requirements need to be carefully considered to meet all GPS requirements. First, GPS systems transmit a right-handed circularly polarized (RHCP) signal, which transforms to a left-handed circularly polarized (LHCP) signal after reflection from the ground. Hence, the RHCP receiver is required to minimize polarization losses, and should have a high cross-polarization rejection ratio to reduce the effect of multipath signals. The latter requirement forces the radiation pattern of the GPS receiver to have a hemispherical coverage in the upper-half plane to receive all the satellite signals, and must have a very sharp slope near the horizon to reject the multipath signals. Keeping in mind that the signal to noise ratio of the received signal is very weak, a considerably good impedance matched receiver is another important issue in the design. In addition, since there are two operating frequencies in the GPS system, L1(1.575 GHz) and L2(1.227 GHz), it would be a very substantial accomplishment if we could design a dual band right-handed circularly polarized GPS receiving antenna.

The printed antenna (microstrip, cavity backed, dipole, etc.) is one of the most popular antennas used for GPS applications. Microstrip antennas have several ad-

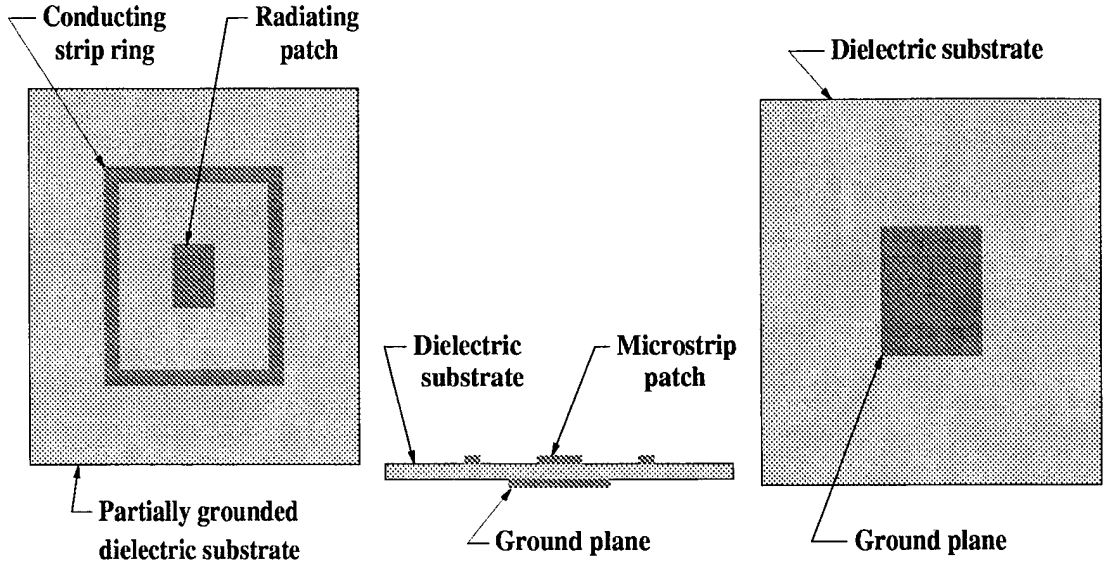

(a) Top View (b) Side View (c) Bottom View

Figure 1.1: Design II : Circularly polarized microstrip antenna with metallic ring around the patch and ground plane

vantages compared to conventional microwave antennas, such as low profile planar configurations which can be made conformal, low scattering cross section, low fabrication cost, potential for dual band operation, linear or circular polarization, etc [2]. Previously, the design of a reconfigurable GPS antenna has been investigated. Figure 1.1, referred to as Design II, illustrates a circularly polarized antenna with a small ground plane developed in [3, 4, 5, 6]. Some parametric studies, such as ring width and ring separation, have been carried out in previous reports to obtain an optimal design. In this report, we continue focusing on this antenna because there are several issues that still require further study. For example, it is not well understood how the size of the ground plane, parasitic ring, dielectric substrate as well as its thickness modify the far zone radiation pattern. Another important issue is the reduction of the overall size of the antenna.

To conduct all the above parametric studies, we need an accurate full wave EM solver. We have developed a computer code based on the Finite Difference Time Domain (FDTD) method. Although this code is reasonably accurate, it requires improvements in the calculation of the input impedance for probe-fed microstrip

antennas. Another major improvement is needed to compute the input impedance and radiation pattern of a patch with thin slots. These slots are needed to decrease the overall size of the antenna. Another very important issue that needs to be addressed is the performance of this type of antenna in the presence of jamming signals.

This report is organized as follow. Chapter 2 discusses the parametric studies conducted for the antenna depicted in Figure 1.1. Chapter 3 considers the role that the rings plays in modifying the radiation pattern. This particular study is conducted by examining the surface currents induced on the ring. In this chapter we briefly discuss a scheme to reduce the overal size of the ring as well as compare the behavior of this reconfigurable antenna with the well known Yagi-Uda array. Chapter 4 addresses the improvements that have been made to our FDTD code. Chapter 5 discusses the performance of a reconfigurable antenna (Design I) in the presence of jamming signals. It also discusses the coverage of the antenna as a function of gain and the trade offs that will be necessary to obtain an antenna that has good coverage and at the same time can diminish the impact of jamming signals incident from directions around the horizon. We conclude with Chapter 6 where a summary of the work performed is given as well as plans for future work.

1.2 Technology Transition

- Customer: Mr. Todd Jenkins
  AFRL/SNAR
  Reference Systems Branch
  2241 Avionics Circle Suite 19
  WPAFB OH 45433-7321

  Voice: (937)255-5668 / DSN 785-5668 x4138
  Fax: (937)656-4301 / DSN 786-4301
  E-mail: Todd.Jenkins@sn.wpafb.af.mil

- Results: Study of reconfigurable printed antenna element

- Application: Antenna for GPS applications in the presence of jamming signals

Chapter 2

Circularly Polarized Antenna - Small Ground Plane

The design procedure for circularly polarized rectangular microstrip antennas can be found in the literature [7, 8, 9]. However, in order to make the antenna reconfigurable, a set parasitic rings and or strips has to be designed. In a previous study [3, 5, 4], a scheme for controlling the radiation pattern of a circularly polarized microstrip antenna was presented. It consists of a microstrip antenna with a metallic ring around the radiating patch as shown in Figure 2.1. By adding the ring, which is loaded with switches [10], it is possible to change the characteristics of the surface waves, and thus the radiation field pattern can be modified [11, 12]. This type of antenna is referred to as a reconfigurable antenna. A parametric study is conducted to determine the effect of various parameters (dimensions of ground plane, ring and substrate as well as substrate thickness) on the radiation pattern. This parametric information is very critical in terms of antenna design. Hence, in this report, we are trying to determine the optimal dimensions of the ground plane, ring and substrate.

The proposed GPS antenna receives right-hand circularly polarized (RHCP) field, and hence, it is convenient to plot the antenna pattern in terms of two orthogonal components E_{RHCP} and E_{LHCP} (left hand circularly polarized) , namely,

$$\vec{E} = E_{RHCP}\,\hat{e}_R + E_{LHCP}\,\hat{e}_L = \frac{E_\theta + jE_\phi}{\sqrt{2}}\,\hat{e_R} + \frac{E_\theta - jE_\phi}{\sqrt{2}}\,\hat{e_L}, \tag{2.1}$$

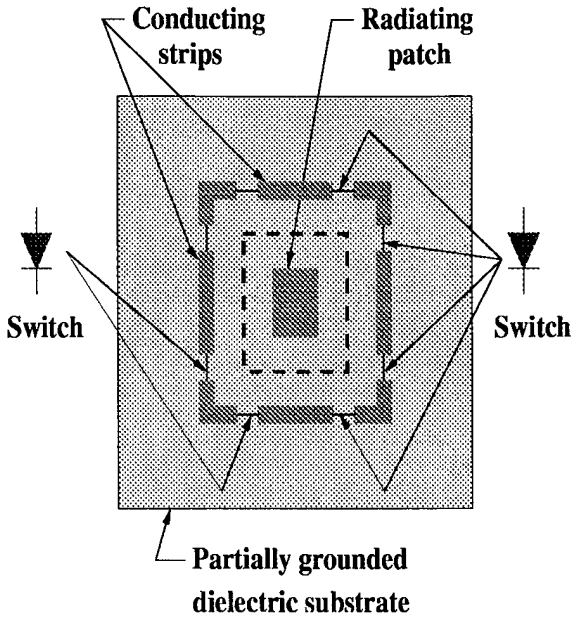

Figure 2.1: Circularly polarized microstrip antenna with small ground plane and diode-loaded metallic ring around the patch (top view)

where E_θ and E_ϕ are the far-field radiated fields in the θ and ϕ directions, respectively. The unit complex vectors $\hat{e}_R$ and $\hat{e}_L$ are given by

$$\hat{e}_R = \frac{\hat{\theta} - j\hat{\phi}}{\sqrt{2}} \tag{2.2}$$

and

$$\hat{e}_L = \frac{\hat{\theta} + j\hat{\phi}}{\sqrt{2}} \tag{2.3}$$

Before we present numerical results it is important to mention that the antenna is fed by two probes located along the diagonal. Two probes are used to obtain a symmetric pattern. Furthermore, unless otherwise indicated, the relative dielectric constant is assumed to be equal to $\epsilon_r = 9.2$ and the width of the metallic ring is approximately $0.63cm$.

2.1 Parametric Study - Ring Size

In this study, it is found that the overall size of the metallic ring is a critical design parameter. The antenna patterns of a $RHCP$ microstrip antenna (with substrate

thickness h equals to 0.8 cm or 0.127 λ_d at L_1) loaded with a ring of various dimensions ($S_1 \times S_2$) are shown in Fig. 2.2. Note that S_1 and S_2 are measured from the center of the patch antenna to the inner edges of the ring. It is clearly seen that the main-beam of the antenna pattern becomes wider as the ring size increases. On the other hand, when the dielectric thickness h of the antenna is 0.27 cm (0.043 λ_d), the main beam becomes narrower when the ring size increases as depicted in Fig. 2.4. Figure 2.6 illustrates another case when the dielectric thickness is even thinner, namely, 0.13 cm or 0.021 λ_d. Note that the pattern does not change very much when the ring dimensions change. The surface wave is weak for antennas mounted on a (electrically) thin dielectric substrate, and hence, the induced electric surface current on the ring is small. These examples show that the substrate has to be thick so the surface waves excited within the substrate are strong and can be manipulated to modify the overall pattern of the antenna. The cross polarized components (LHCP) are also depicted in Figures 2.3, 2.5 and 2.7. Note that these components are at lower level than the RHCP components. They do become smaller when the substrate thickness decreases. This suggests a trade-off has to be made between low cross polarization and a reconfigurable radiation pattern.

Note also that the dimensions of the microstrip antenna in each of the three cases are different because the resonant size of a microstrip antenna depends on the substrate thickness.

2.2 Parametric Study - Ground Plane Size

In this section, the effect of the size of the metallic ground plane, placed underneath the dielectric substrate, on the overall antenna performance is studied. For the case of $h = 0.12\lambda_d$, the antenna patterns corresponding to different ground plane dimensions are similar except when the ground plane is the same size as the substrate as shown in Fig. 2.8. However, it is important to note that for Design II, the ground plane has to be smaller than the ring. Otherwise, the antenna will not be reconfigurable. If the ground plane is the same size or larger than the ring, the surface waves within the dielectric become weak and cannot be used to modify the beamwidth of the antenna.

Note that the ground plane needs to be larger than the patch antenna. The cross polarized component (LHCP) is depicted in Figure 2.9. The pattern does change as the size of the ground plane changes, however, it remains below -30 dB for all cases considered here.

2.3 Parametric Study - Substrate Size

The effect of the substrate size on the antenna performance is of second order as shown in Fig. 2.10. However, when the substrate size decreases to a value close to the overall size of the metallic ring, the antenna pattern changes drastically. This is expected because the field interaction between the edge of the substrate and the metallic ring becomes stronger. This case is not examined in this study; however, it will be addressed in the future. The cross polarized component (LHCP) is shown in Figure 2.11. As in the previous case, it remains below -30 dB as the size of the substrate changes.

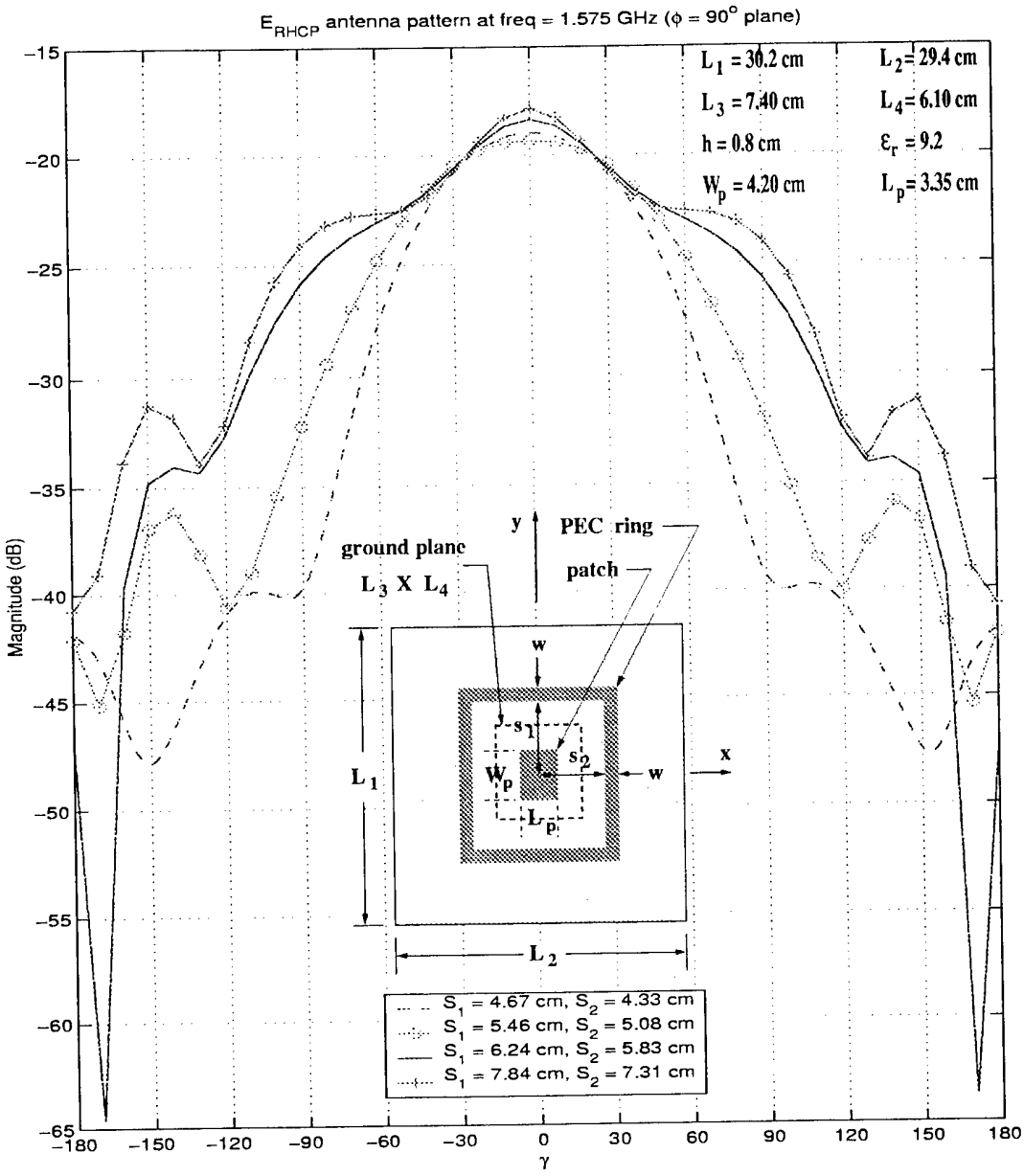

Figure 2.2: Calculated E_{RHCP} antenna pattern at $L1$ in $y-z$ plane of a RHCP antenna ($h = 0.8$ cm) loaded with a metallic ring with size $S_1 \times S_2$.

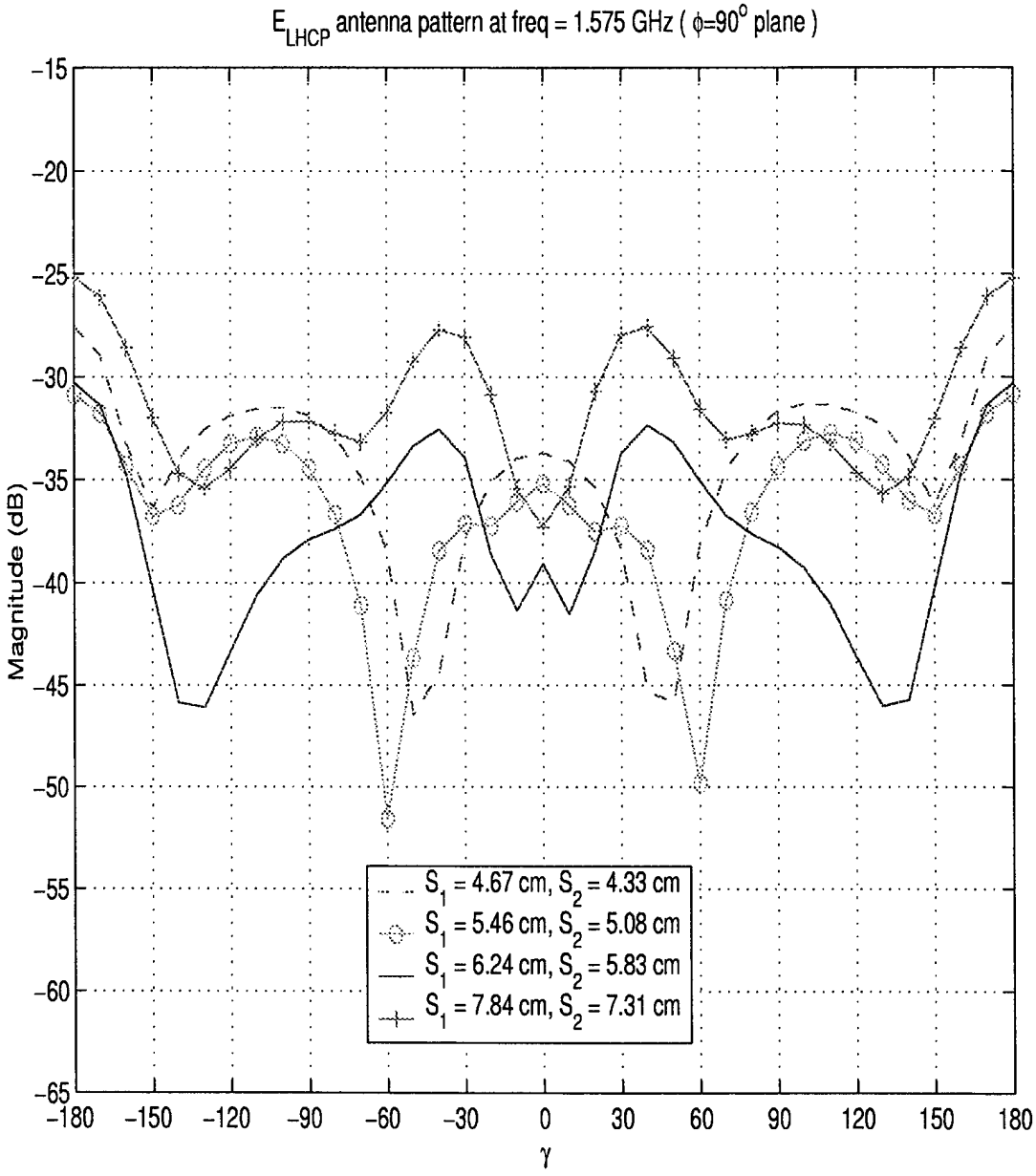

Figure 2.3: Calculated E_{LHCP} antenna pattern at $L1$ in $y-z$ plane of a RHCP antenna ($h = 0.8$ cm) loaded with a metallic ring with size $S_1 \times S_2$.

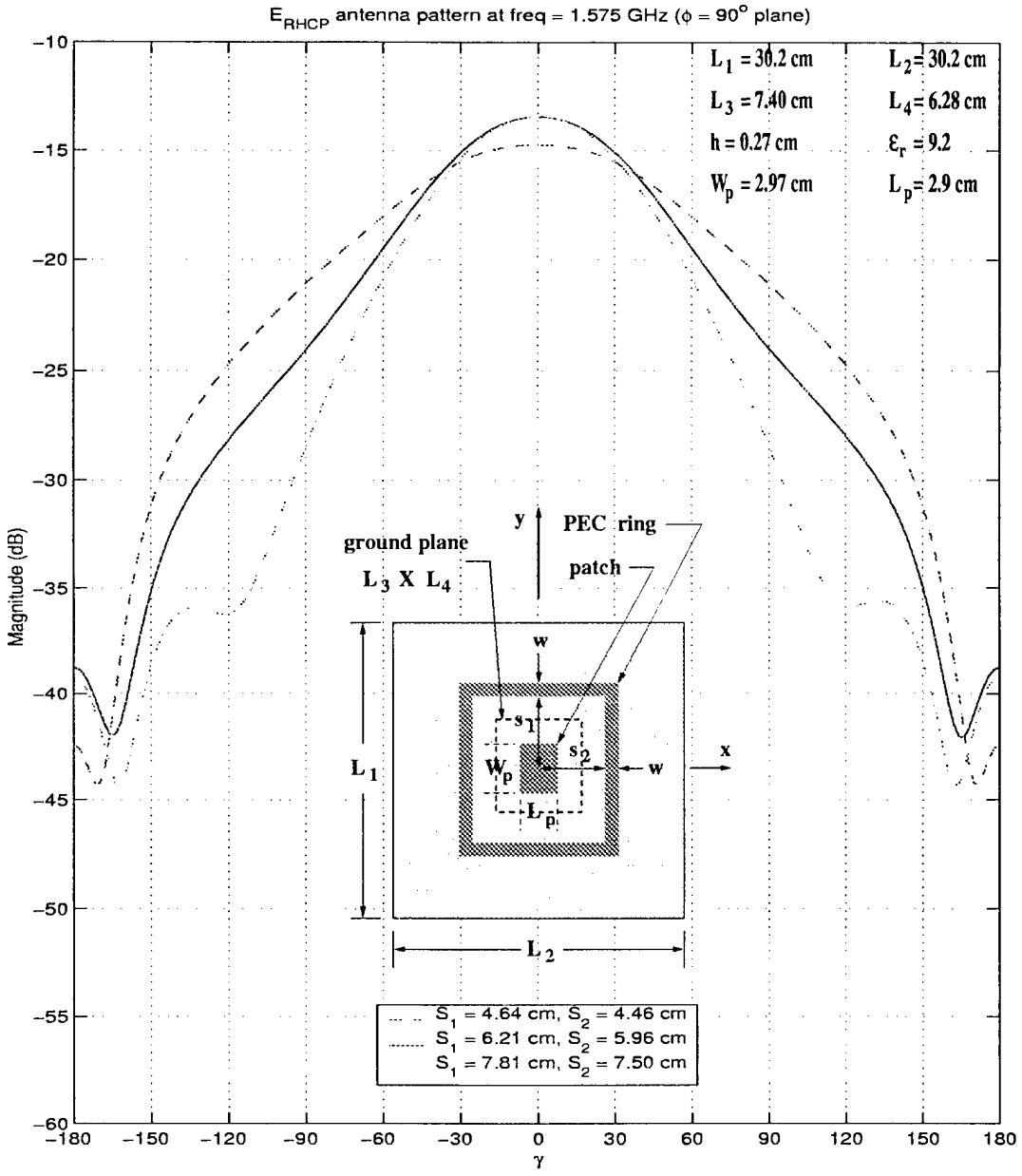

Figure 2.4: Calculated E_{RHCP} antenna pattern at $L1$ in $y-z$ plane of a RHCP antenna ($h = 0.27$ cm) loaded with a metallic ring with size $S_1 \times S_2$.

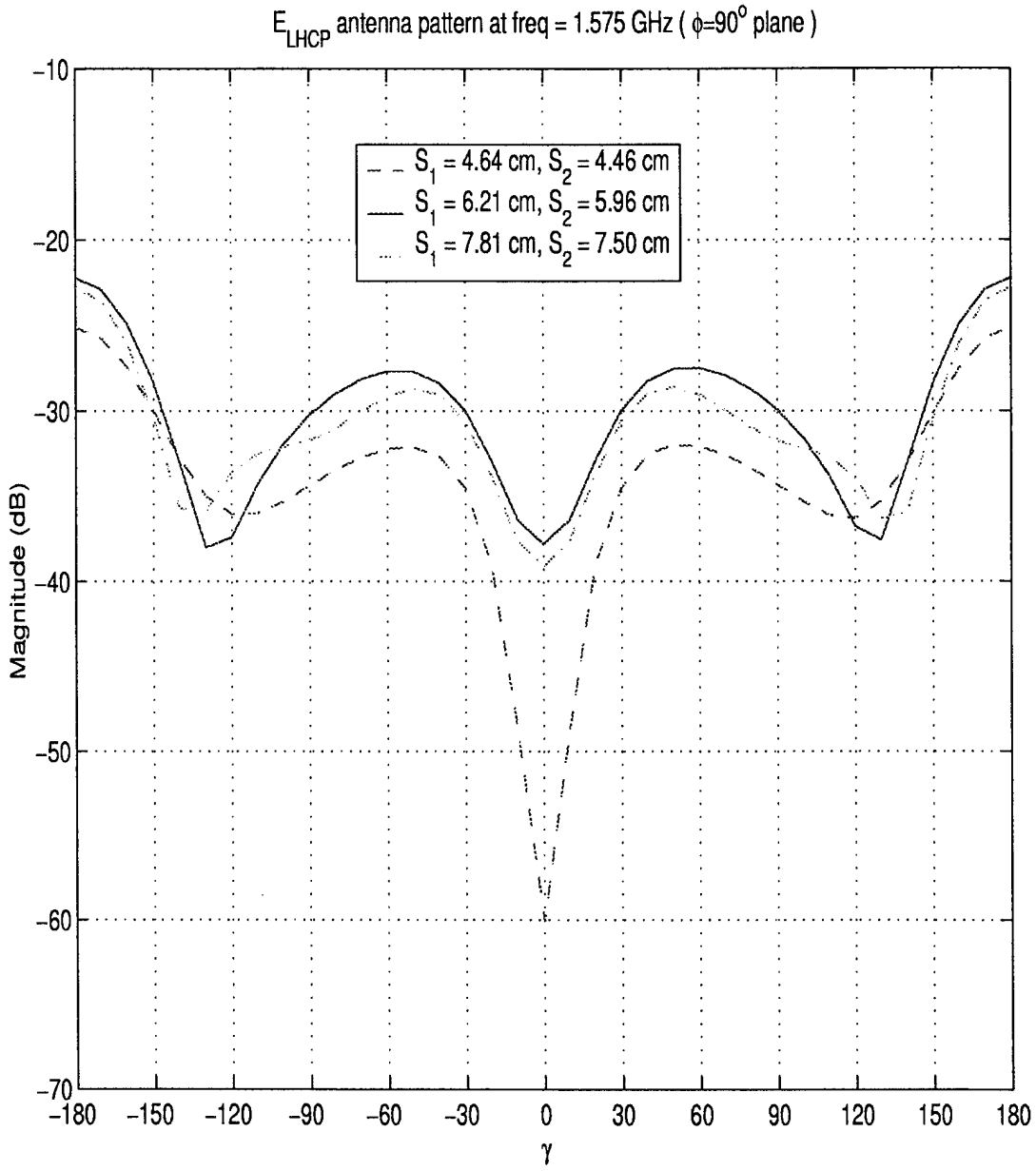

Figure 2.5: Calculated E_{LHCP} antenna pattern at $L1$ in $y-z$ plane of a RHCP antenna ($h = 0.27$ cm) loaded with a metallic ring with size $S_1 \times S_2$.

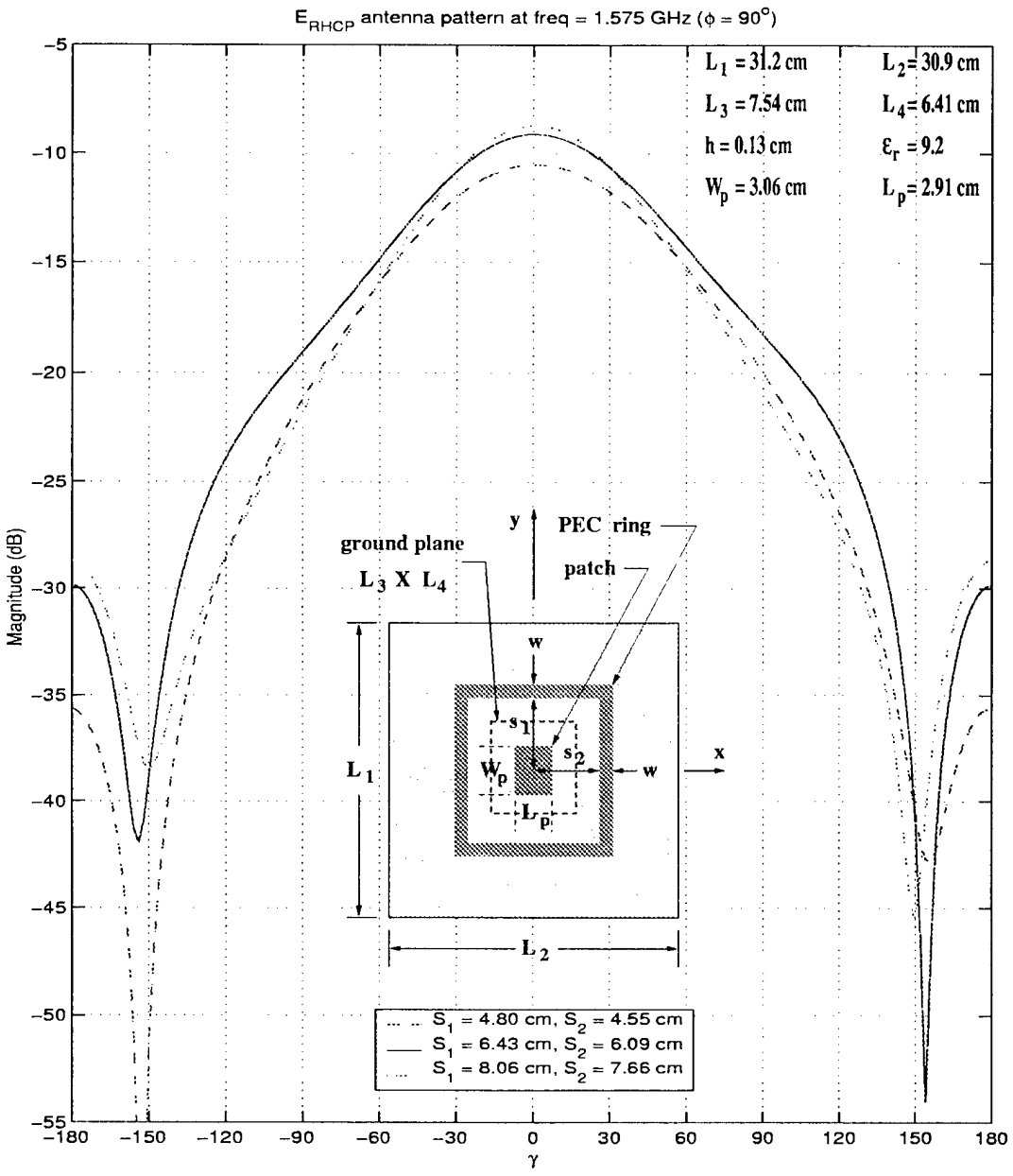

Figure 2.6: Calculated E_{RHCP} antenna pattern at $L1$ in $y-z$ plane of a RHCP antenna ($h = 0.13$ cm) loaded with a metallic ring with size $S_1 \times S_2$.

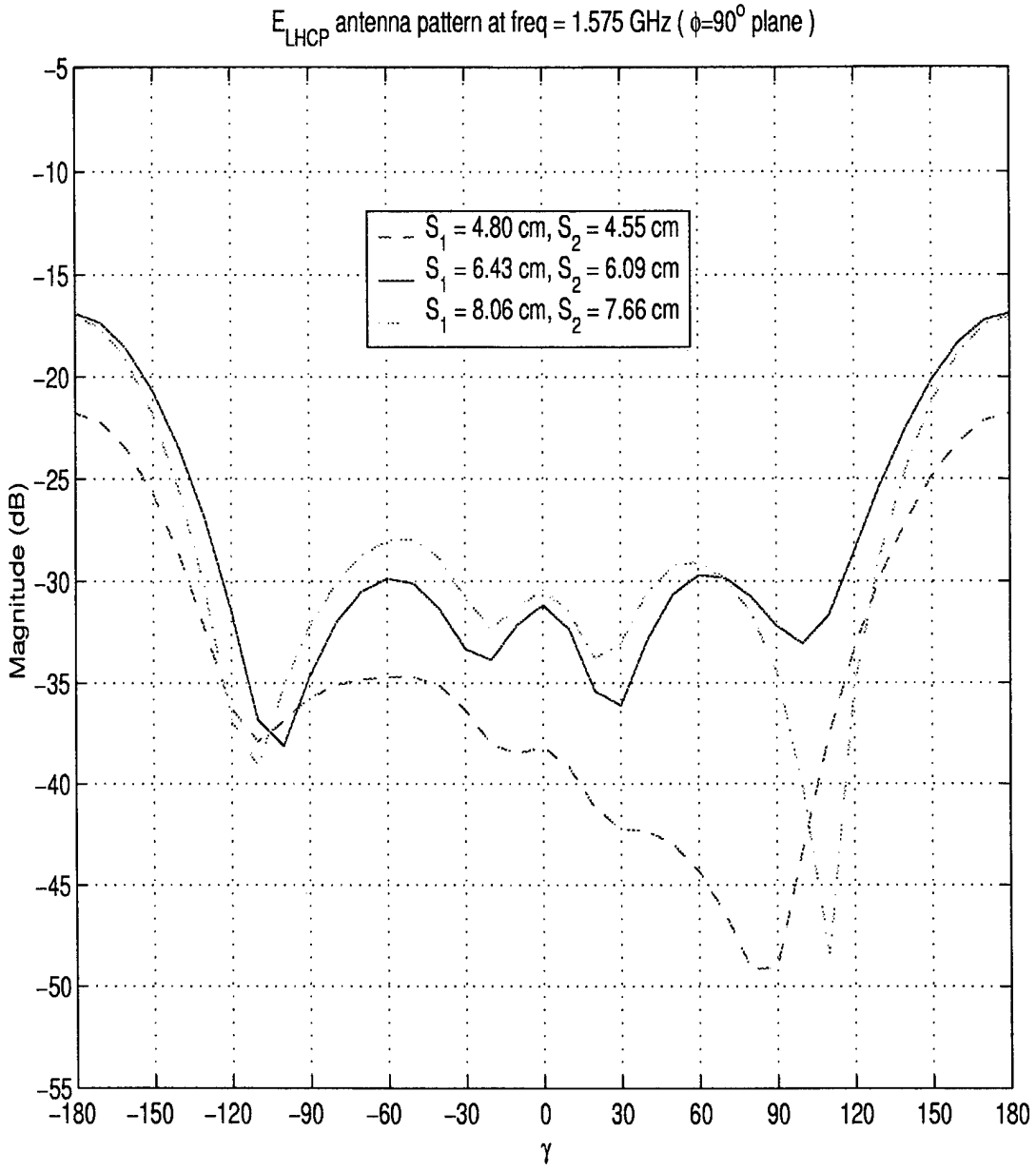

Figure 2.7: Calculated E_{LHCP} antenna pattern at $L1$ in $y-z$ plane of a RHCP antenna ($h = 0.13$ cm) loaded with a metallic ring with size $S_1 \times S_2$.

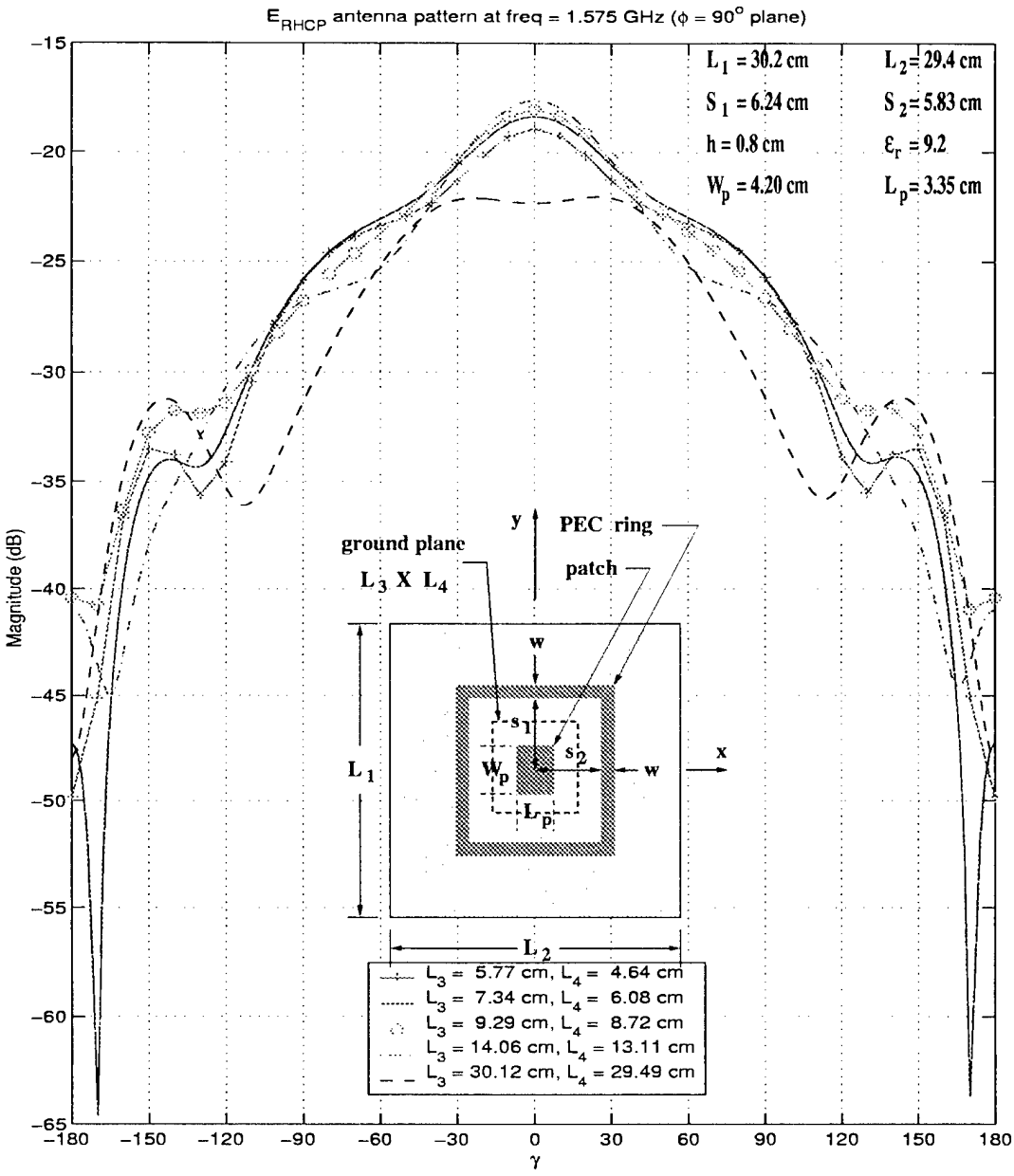

Figure 2.8: Calculated E_{RHCP} antenna pattern at $L1$ in $y-z$ plane of a RHCP antenna loaded with a metallic ring with different ground plane dimensions $L_3 \times L_4$.

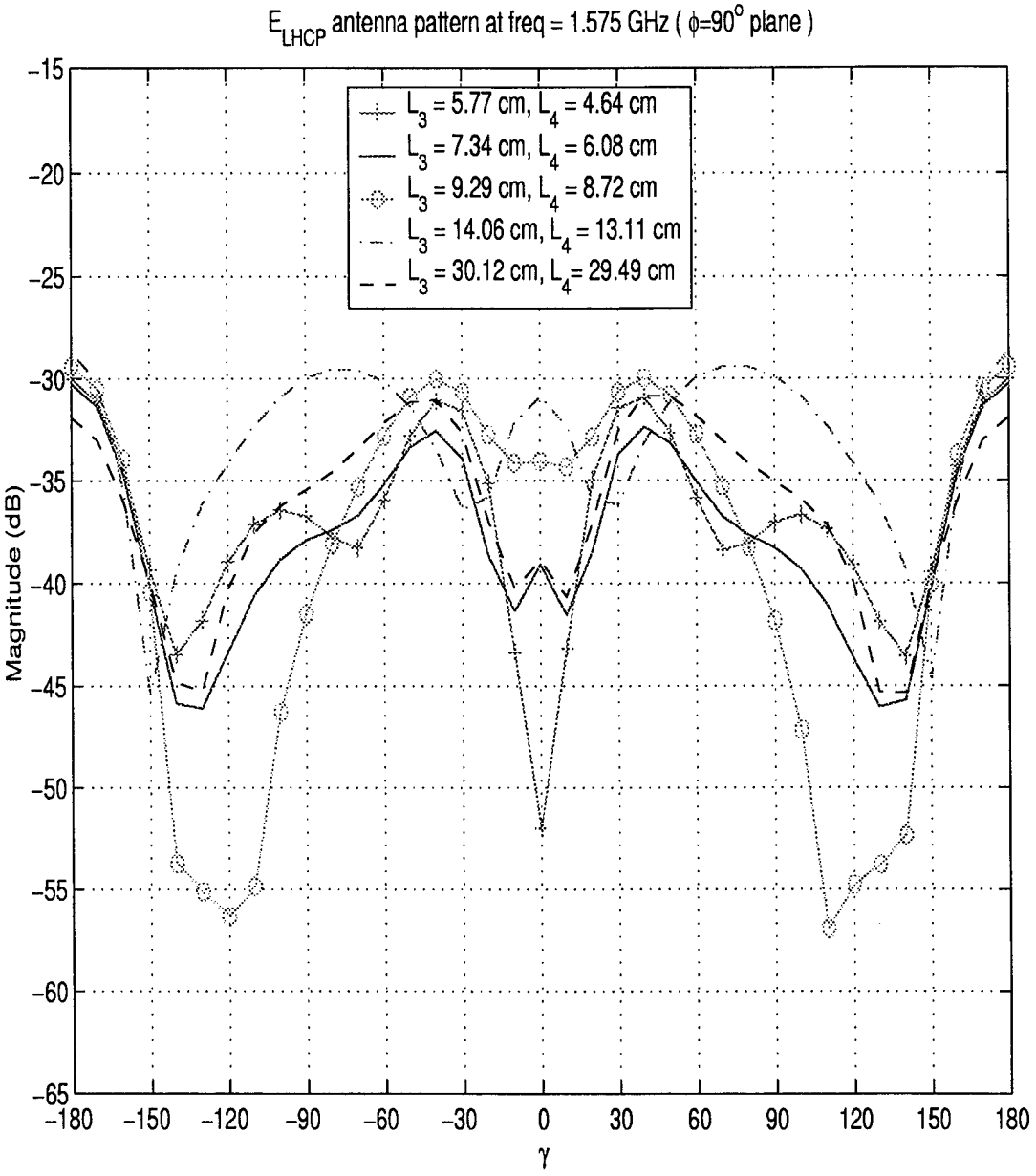

Figure 2.9: Calculated E_{LHCP} antenna pattern at $L1$ in $y-z$ plane of a RHCP antenna loaded with a metallic ring with different ground plane dimensions $L_3 \times L_4$.

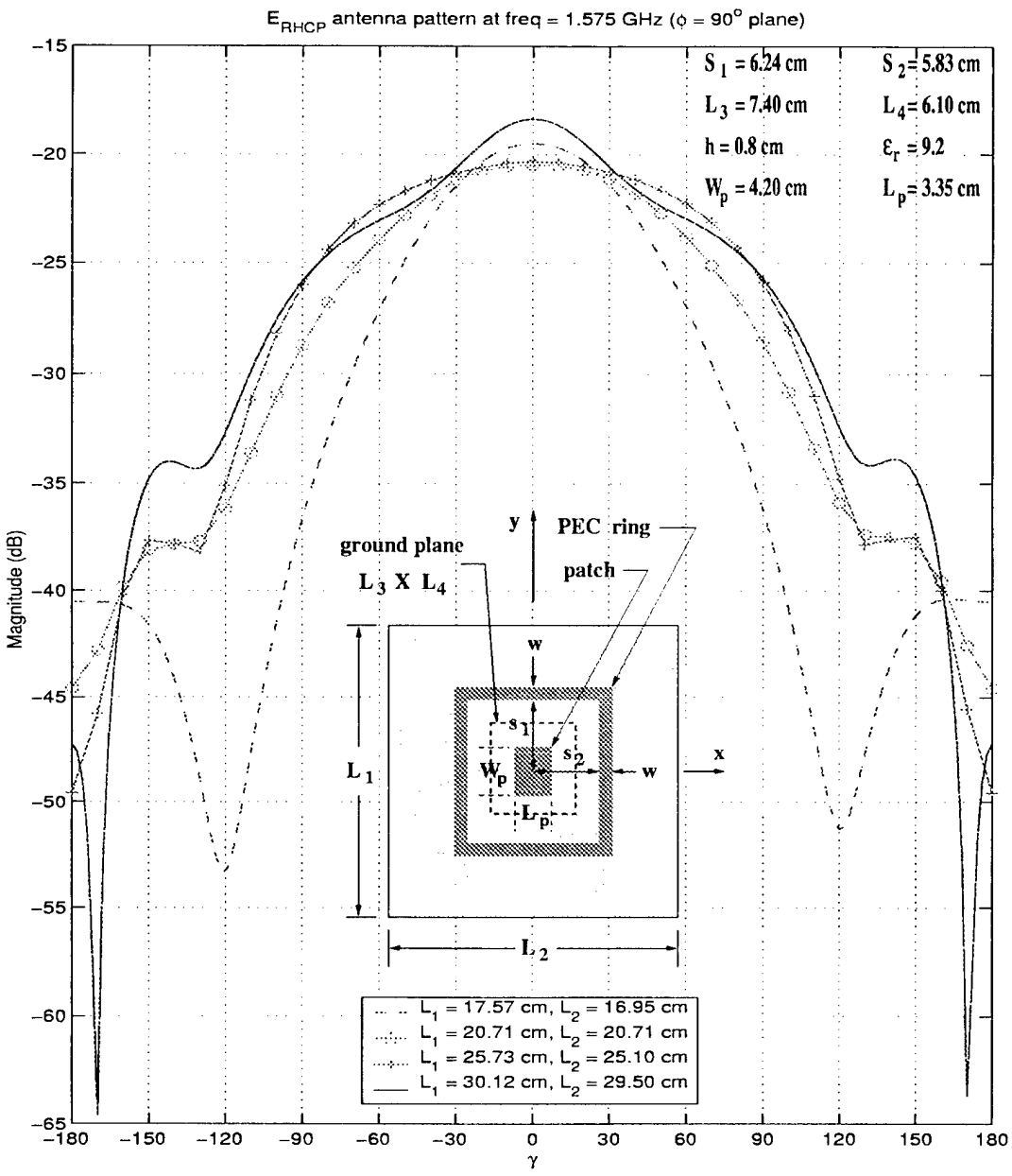

Figure 2.10: Calculated E_{RHCP} antenna pattern at $L1$ in $y-z$ plane of a RHCP antenna loaded with a metallic ring with different substrate dimensions $L_1 \times L_2$.

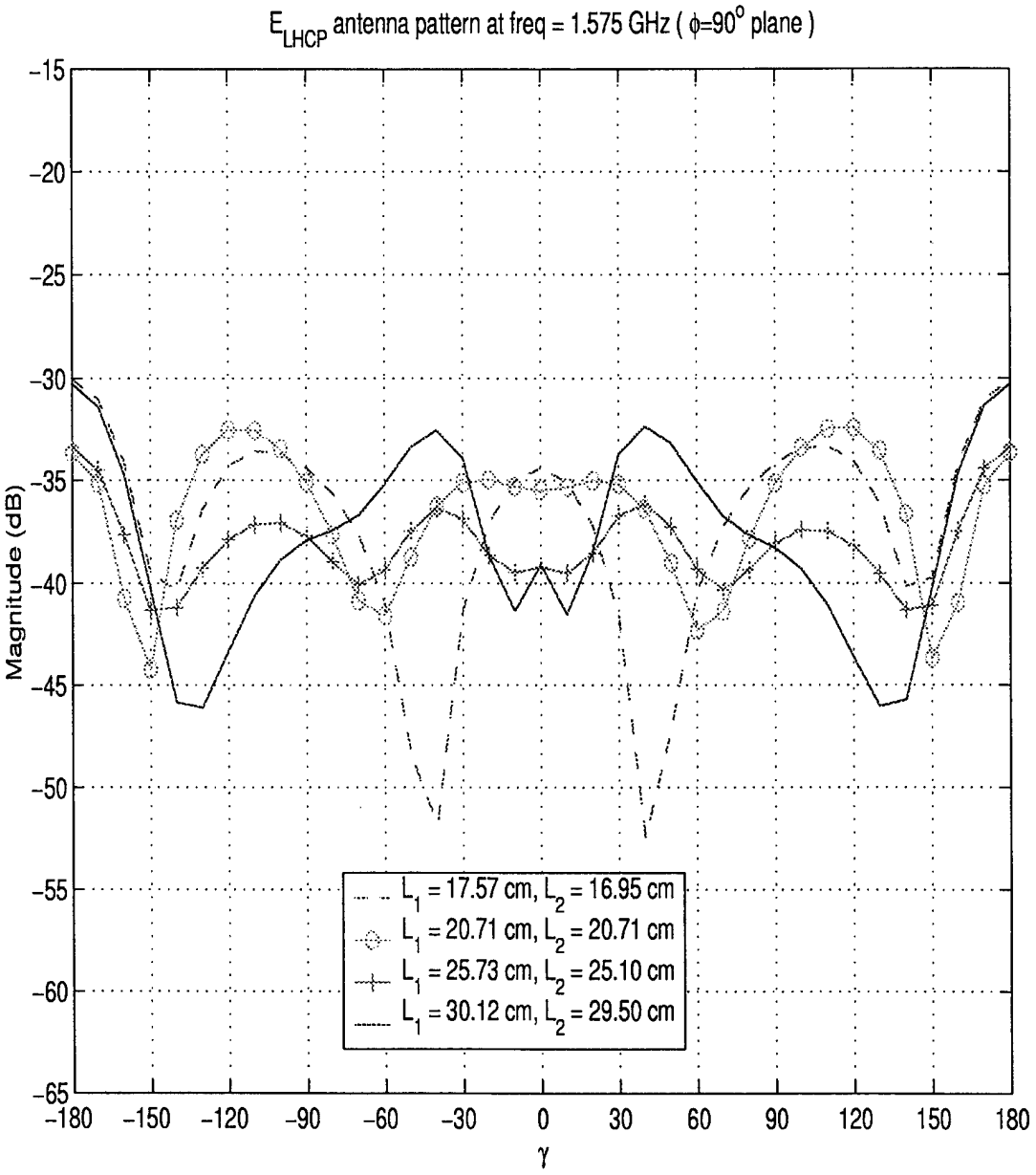

Figure 2.11: Calculated E_{LHCP} antenna pattern at $L1$ in $y-z$ plane of a RHCP antenna loaded with a metallic ring with different substrate dimensions $L_1 \times L_2$.

Chapter 3

Surface Current Analysis

In this chapter, the proposed antenna configuration (Fig. 3.1(a)) is examined through the study of the induced electric currents on the metallic ring to provide a better understanding of the antenna radiation mechanisms. Keeping in mind that a Yagi Uda array also employs parasitic elements, a comparison of the behavior of these two antennas is performed to point out some of the differences in their behavior. A possible way to reduce the overall ring size is also discussed in the last section.

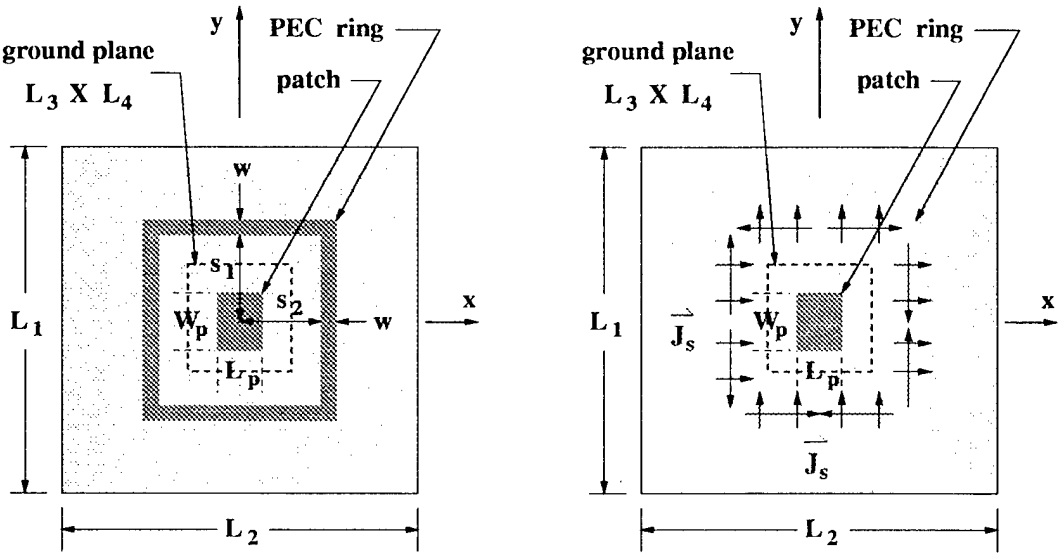

Figure 3.1: Induced surface current model. (a) Original ring structure. (b) Induced surface currents.

The metallic ring creates a tangential ($x-y$ plane) magnetic field discontinuity and a zero tangential electric field across its area. This boundary condition can be modeled by induced electric and magnetic current sources. The induced magnetic current source $\vec{M}_s$ has a zero magnitude due to a zero tangential electric field on the conductor. On the other hand, the tangential components (x- and y- directions) of the magnetic field are discontinuous across the metallic ring by an amount equal to an induced surface electric current source $\vec{J}_s$ given by

$$\vec{J}_s = \hat{z} \times (\vec{H} - \vec{H}_d), \tag{3.1}$$

where $\vec{H}$ and $\vec{H}_d$ are the magnetic fields above (air region) and below (dielectric region) the ring, respectively.

3.1 Analysis of Induced Surface Currents

In this section, the metallic ring structure is examined through the study of the induced currents on the patch antenna and ring. Since the effect of the ring dimensions on the radiated field is more significant than that of the other parameters, only this case is considered. As in Chapter II, the dielectric constant of the substrate is 9.2 and the width of the ring is approximately 0.63 cm.

The analysis begins by noting that the radiated field in one of the principle planes (i.e. $y-z$ plane or $x-z$ plane) can be modified with a pair of metallic strips placed orthogonal to that plane (i.e. along $x-$ direction for $y-z$ plane and along $y-$ direction for $x-z$ plane) as shown in Figures 3.2 and 3.3. In addition, the field contribution due to the presence of the strips is mainly on the E_ϕ components as shown in Fig. 3.4. Therefore, the analysis can be simplified to investigate the behavior of the induced currents on the pair of strips.

Considering the case shown in Fig. 3.2, the induced surface currents (on both strips and microstrip antenna) J_{sx} and J_{sy} are shown in Fig. 3.5 and Fig. 3.6 (a smaller scale). Note that the induced current on the antenna is almost the same with and without strips, and the patch current is much stronger than the induced strip currents. Notice that the strip currents in the $y-$direction are in phase with the

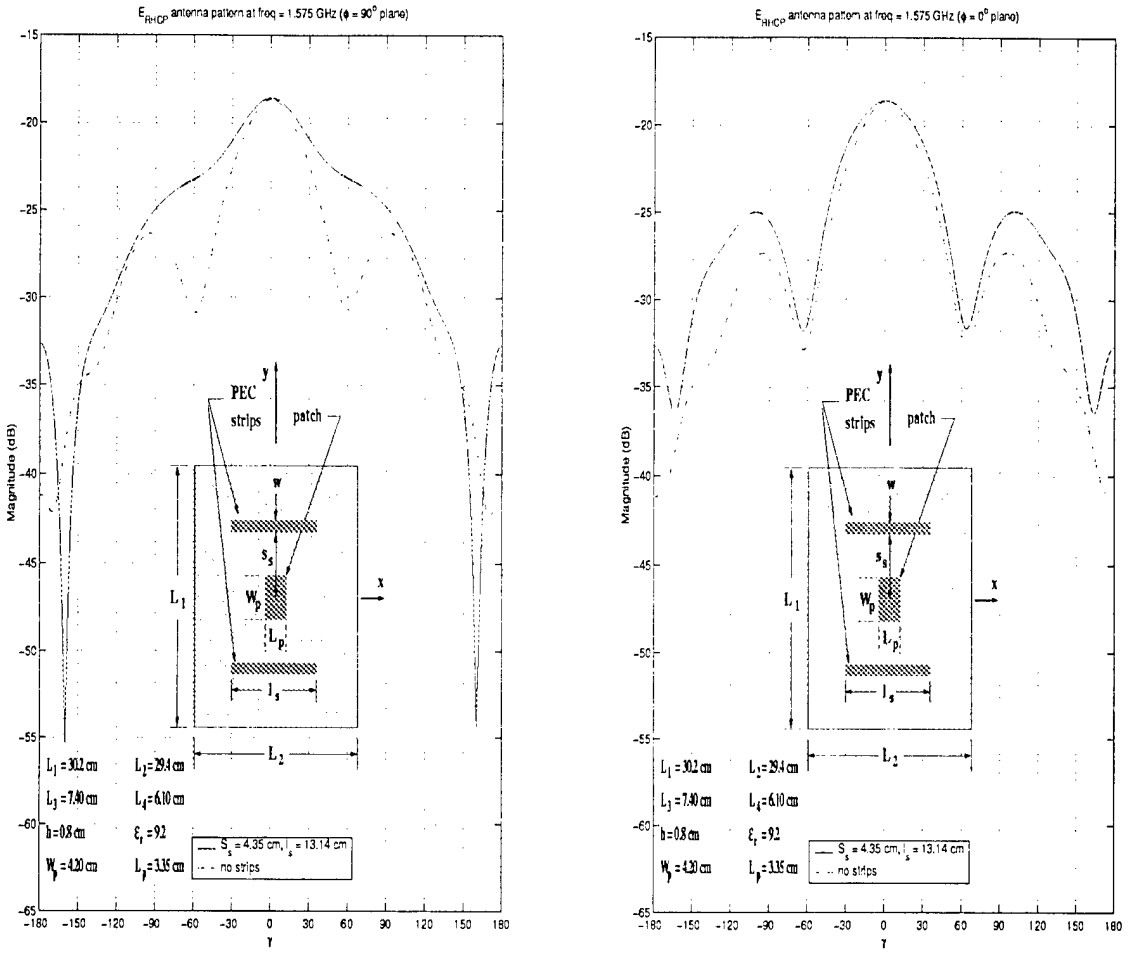

(a) (b)

Figure 3.2: Calculated E_{RHCP} antenna pattern at $L1$ in (a) $y-z$ plane and (b) $x-z$ plane of a RHCP antenna loaded with a pair of metallic strips in $x-$ direction.

$y-$directed patch current. On the other hand, the $x-$directed strip surface currents are out of phase with that of the patch current. Therefore, the in-phase $y-$directed currents contributed to E_θ component are added in the far-field at broadside as shown in Fig. 3.4(b). In this case, the main beam pattern of the strip-loaded case has a slightly higher magnitude and a narrower beamwidth than those of the unloaded case. Considering the induced currents along one of the strips shown in Fig. 3.7, there are two different level current peaks in J_{sx} (right side of the figure) and they are close to being out of phase (almost 180°). This results in a small J_{sx}. On the other strip, another small resultant current flowing in the *same direction* is also produced. With

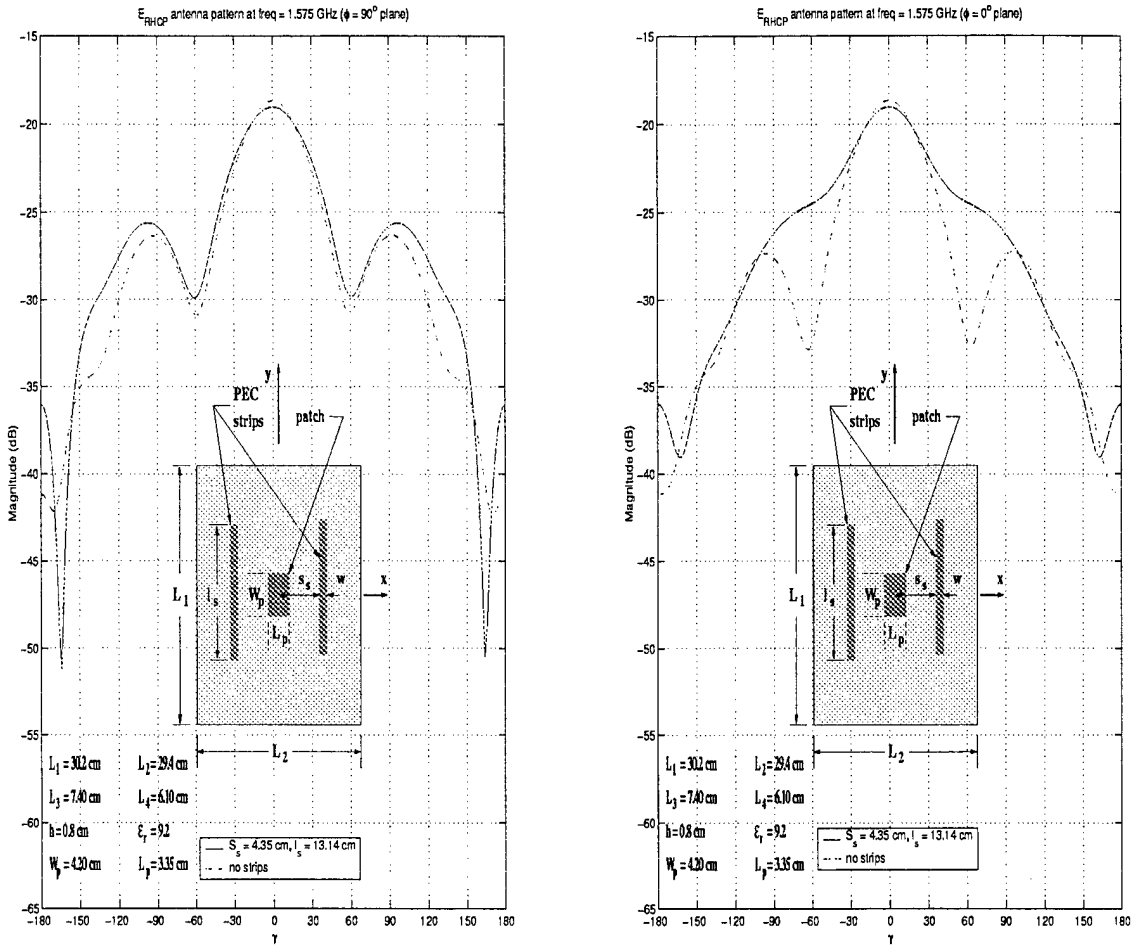

(a) (b)

Figure 3.3: Calculated E_{RHCP} antenna pattern at $L1$ in (a) $y-z$ plane and (b) $x-z$ plane of a RHCP antenna loaded with a pair of metallic strips in $y-$ direction.

the proper magnitudes and phases, these two surface currents contribute to the *nulls* of the E_ϕ component as shown in Fig. 3.4(a).

Next, the J_{sx} and J_{sy} currents on the metallic ring with different ring dimensions (S_1 and S_2) are considered . The J_{sy} currents are given in Fig. 3.8. Notice that the magnitudes of the induced currents decrease as the ring size increases (the inner ring edges are moving away from the patch antenna). This is due to the decrease in coupling between the antenna and the ring as the metallic strips move away from the patch. However, the phase of the J_{sy} currents do not vary significantly. In addition, the phases of the two peaks in the current amplitude (for each case) are

almost the same. Hence, as in the case for the pair strips, the fields radiated by the $y-$directed induced currents on the front and the back strips are added in-phase to the θ component of the field.

The induced current J_{sx} (shown in Fig. 3.9) of the metallic ring behave differently than the $y-$component of the induced current. The magnitude of the current also decreases as the ring size increases. However, the two peaks in each strip are now approximately 180^o out of phase. When the ring is close to the center patch, one of the peaks is larger than the other. This results in a net current flow in the $x-$direction. The effect of this current on the radiated field depends on its strength, and its phase relative to the phase of the microstrip antenna current. In this case, the resultant induced current causes the antenna beamwidth to increase as the ring size increases. When the substrate becomes thinner, namely, $h = 0.27$ cm, the antenna beamwidth decreases when the ring size is increased as shown in Fig. 2.4. The $y-$directed induced current has similar behavior as that of the thicker substrate case. On the other hand, the $x-$directed current has a different effect on the antenna performance. The J_{sx} shown in Fig. 3.10 has one large peak across each side of the ring. The antenna pattern depends on interaction between the field due to this current and the field due to the $x-$directed induced current in the patch antenna. Note that the induced current in this case ($h = 0.27$ cm) has a larger amplitude than the one with a thicker ($h = 0.8$ cm) substrate. Nonetheless, the important fact is the relative magnitude of the induced surface current on the metallic ring compared to the amplitude of the surface current on the center microstrip antenna. For $h = 0.8$ cm, the amplitude of the current on the patch is approximately two times the amplitude of the smallest ring size considered here. For the thinner substrate case ($h = 0.27$ cm), the patch current amplitude is about 20 times larger than the amplitude of the induced current on the ring. When the substrate thickness is further reduced to $h = 0.13$cm, the metallic ring has only a small effect on the radiated field. This is because the magnitude of the induced current is very small compared to that of the microstrip antenna.

3.2 Comparison of Parasitic Ring with Parasitic Elements in Yagi-Uda Array

A Yagi-Uda antenna array, shown in Fig. 3.11 [13, 14], can be considered to be an structure that supports a traveling wave. A typical Yagi-Uda array consists of a source element, a reflector element and a row of directors. Its performance is determined by the current distribution in each parasitic element and the phase velocity of the traveling wave. In other words, the size and spacing of the directors as well as the size and spacing of the reflector have a significant effect on the forward gain, backward gain, and input impedance. In addition, the Yagi-Uda arrays usually have low input impedance and relatively narrow bandwidth (in the order of about 2 %).

There are some similarities between the radiation mechanism of a Yagi-Uda array and the proposed reconfigurable antenna element. Both of them require the use of parasitic element to control the radiated field. The size and spacing of the parasitic elements have a large effect on the radiation characteristics of the antenna. However, the coupling mechanisms between the source element and the parasitics are different. In the Yagi-Uda array, the coupling occurs in free-space, and the source element directly illuminates the parasitic elements (the main beam of the source is pointing towards the parasitics). On the other hand, the coupling is mainly due to surface waves in the proposed structure. This is because the source (center patch element) has a main beam in the broadside direction, and hence, the space-wave coupling between the source and the parasitic ring is weak. Nonetheless, there is a strong surface wave excited by the source due to the electrically thick substrate. Note that rate of decay of the surface wave with respect to distance is smaller than that of the space-wave. In addition, the parasitic elements in a Yagi-Uda array are usually capacitive (the element length is smaller than the length of the source element). This is not the case in the proposed antenna, since the ring surrounds the source element.

Therefore, the basic radiation mechanism, which is the use of parasitic elements to improve the directivity and front-to-back ratio of the source element, is similar

for the Yagi-Uda array and the proposed antenna element. However, the coupling mechanism from the source to the elements is different between the two structures.

3.3 Scheme to Reduce Ring Dimensions

A scheme to reduce the overall ring size is presented in this section. The idea is based on loading the metallic ring with inductive elements to modify its characteristics. First we will explore the use of capacitive elements.

A capacitive loading approach is shown in Fig. 3.12 for the case when $h = 0.8$ cm. By taking out some small portions of the metallic ring, the gap with dimension Δ acts as a capacitor. The solid-line represents the case of a solid ring with an overall size 6.24×5.83 cm^2. The dash-line plot corresponds to a solid ring with an overall size 5.45×5.09 cm^2. By taking some small Δ portions of the larger ring (solid-line case), the antenna patterns for two different dimensions of Δ tend to the smaller ring (dash-line case). This implies that capacitive loads are not helpful in reducing the size of the ring.

On the other hand, by loading the smaller ring with "c" shape elements (notch with depth w and width Δ), the antenna patterns for two different Δ dimensions are similar to the larger ring as shown in Fig. 3.13. By properly adjusting Δ, the new scheme should be able to produce a radiation pattern very close to that of the first (larger) ring. Note that the width of the notch needs to be larger than the width of the center patch for this scheme to function properly. Therefore, an overall size reduction of about 23% is achieved.

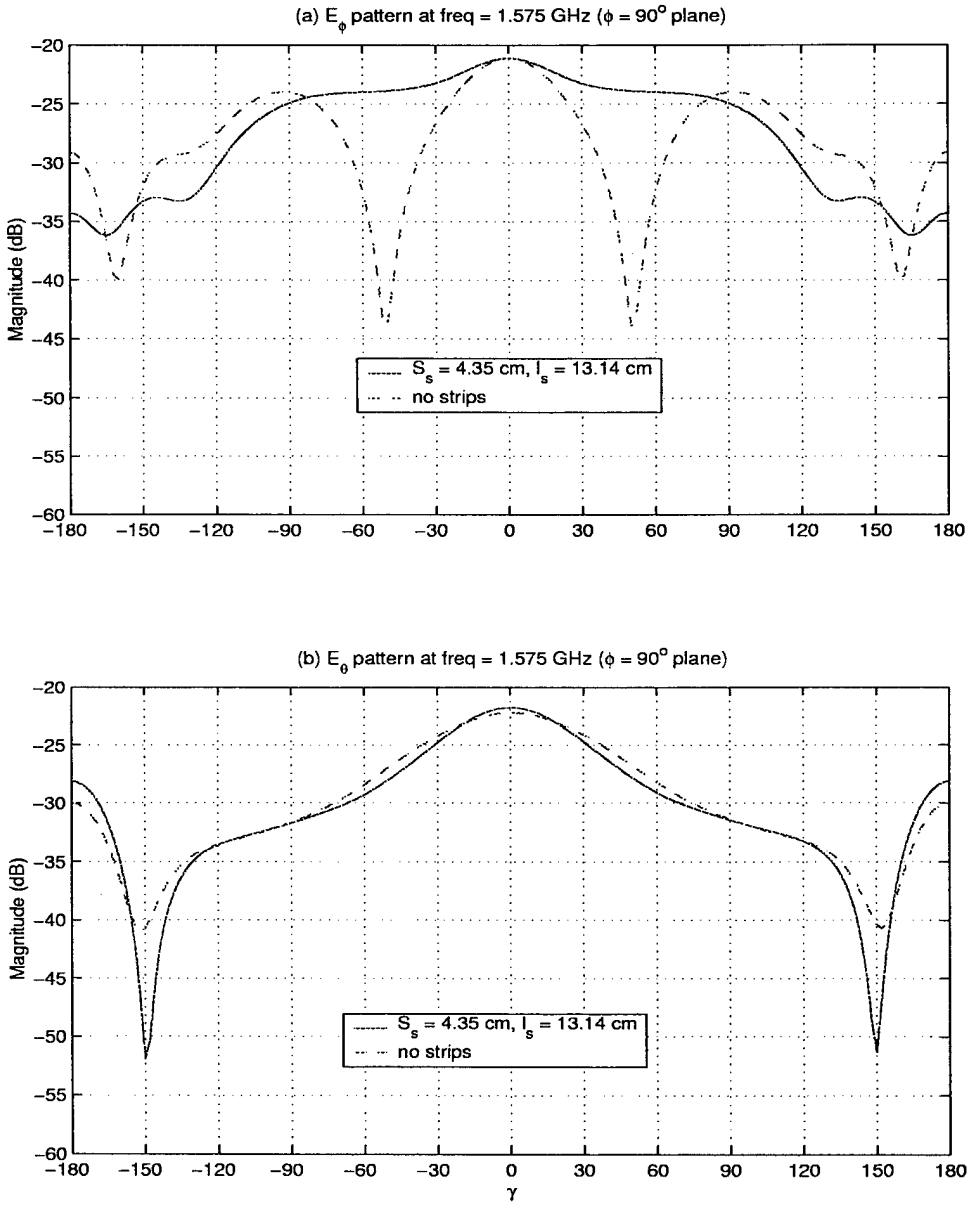

Figure 3.4: Calculated (a) E_ϕ and (b) E_θ antenna pattern at $L1$ of a RHCP antenna loaded with a pair of metallic strips in $x-$ direction as shown in Fig. 3.2.

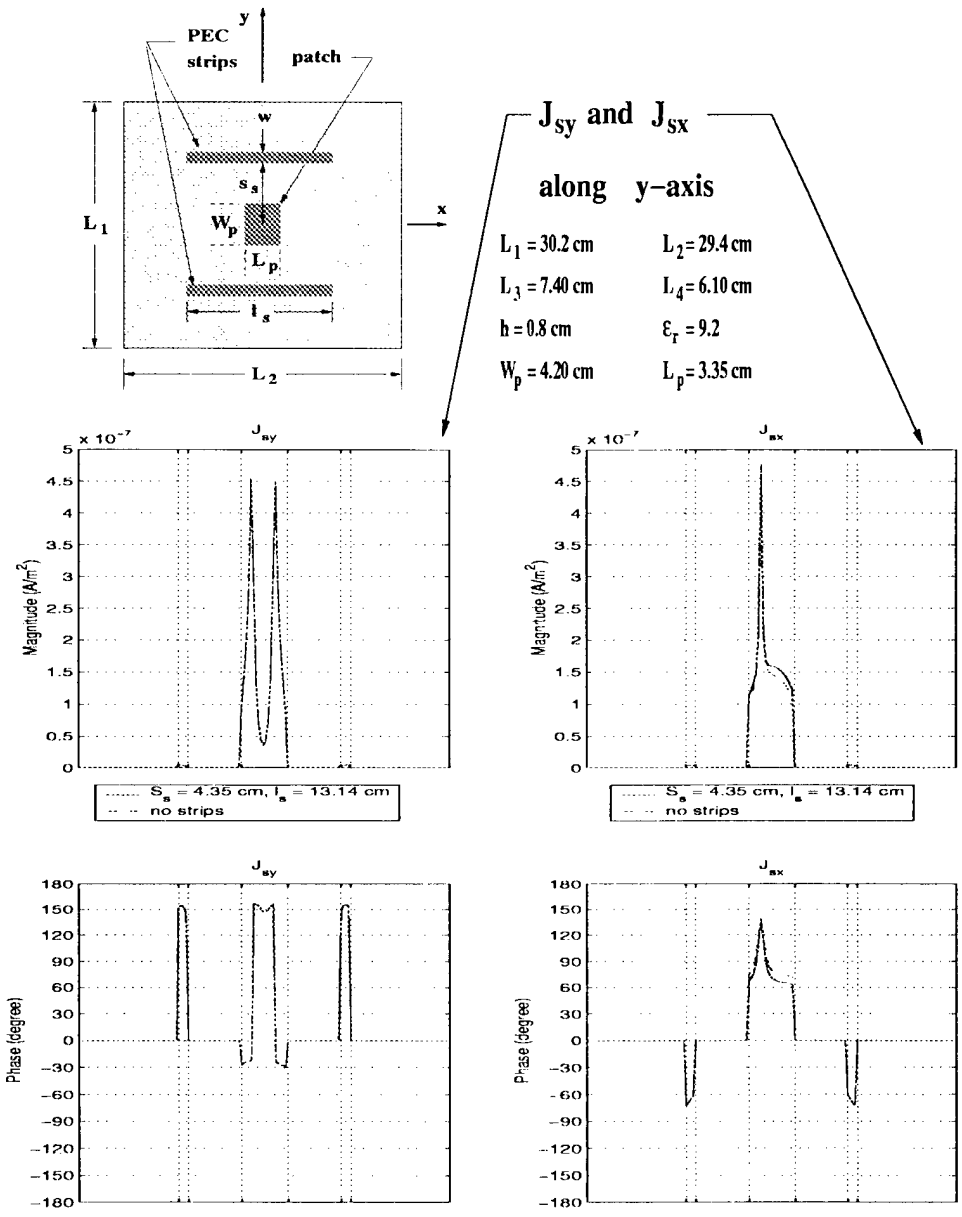

Figure 3.5: Induced surface current J_{sy} (left) and J_{sx} (right).

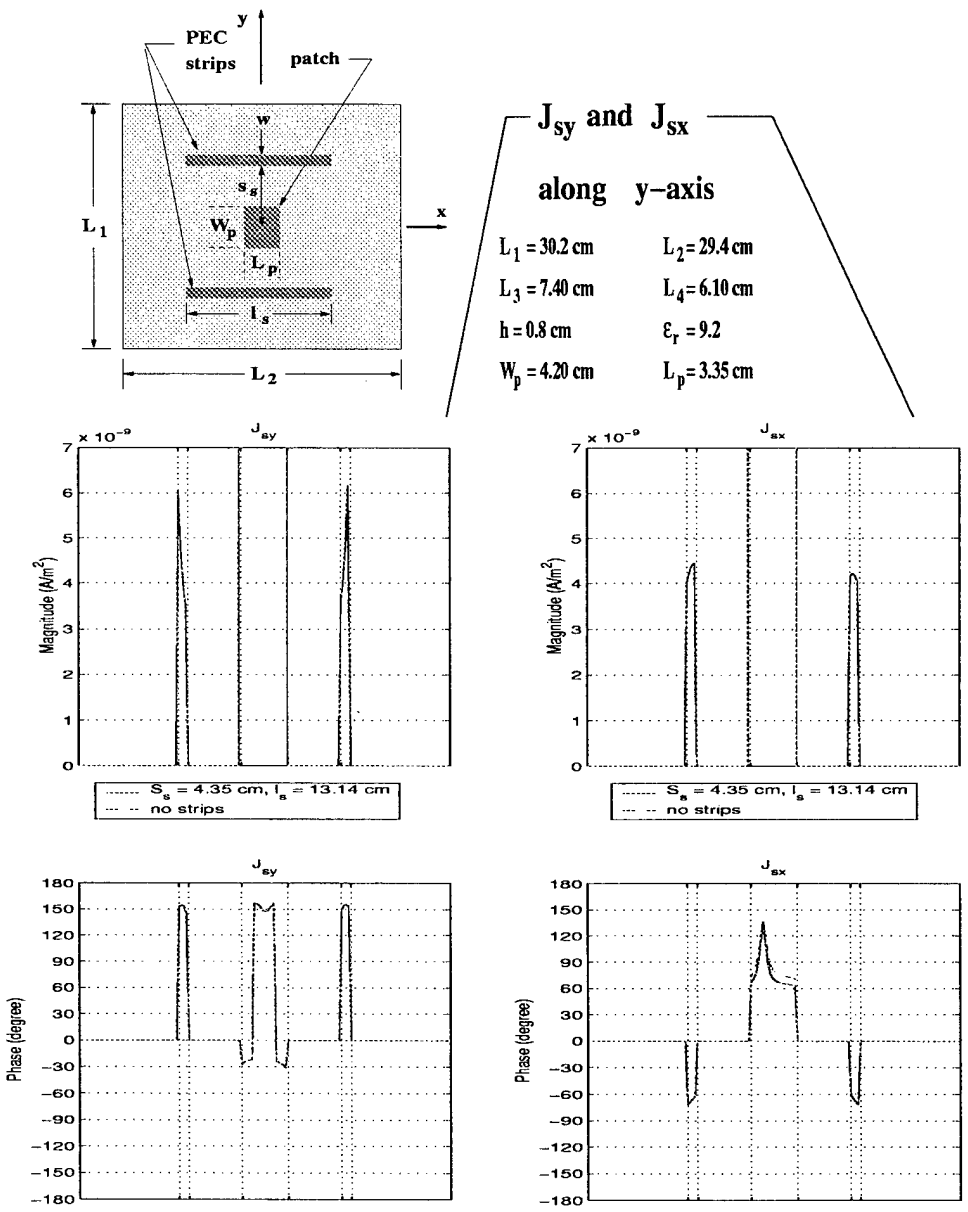

Figure 3.6: Induced surface current J_{sy} (left) and J_{sx} (right) (a smaller amplitude scale to show the strip current amplitudes).

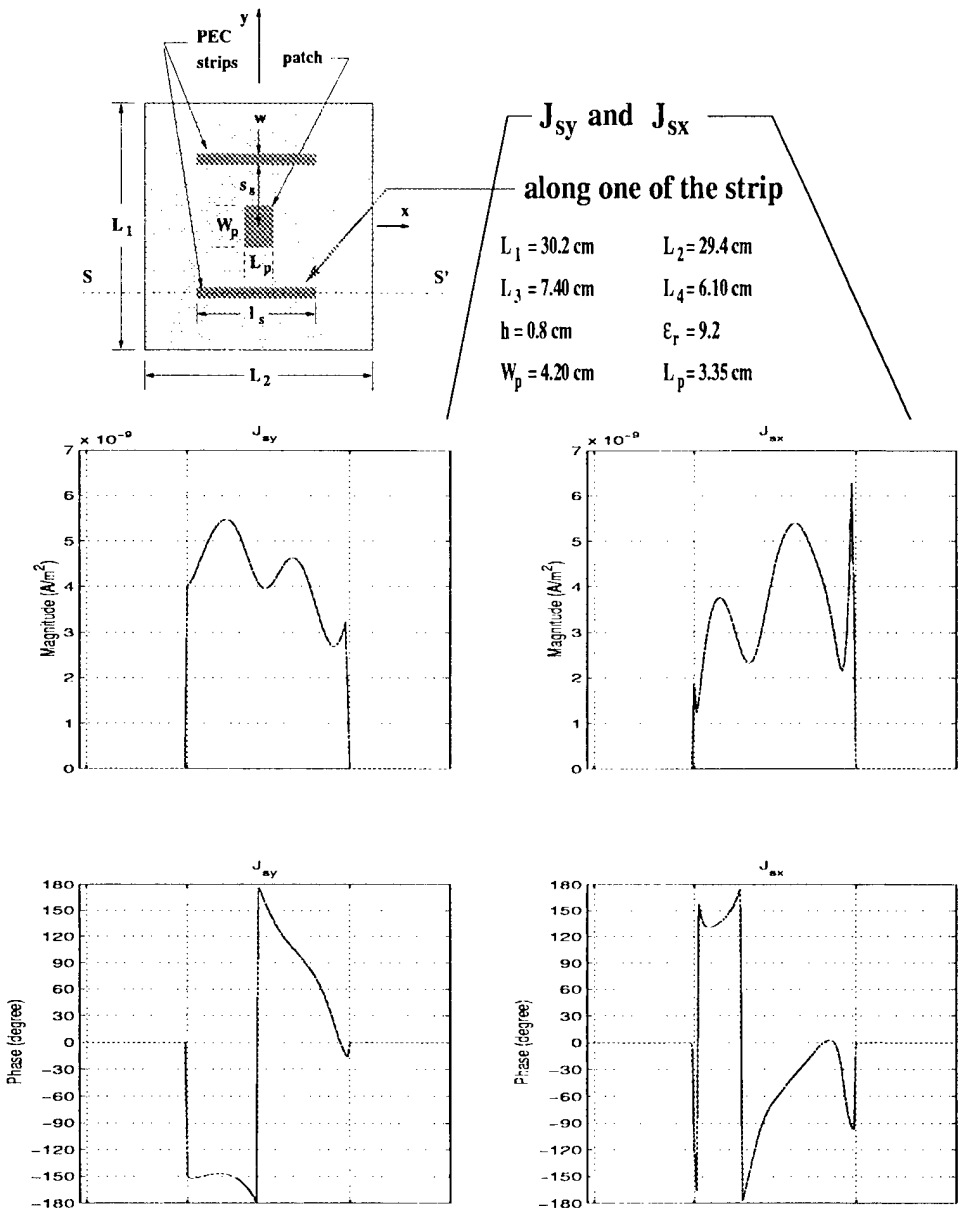

Figure 3.7: Induced surface current J_{sy} (left) and J_{sx} (right) along a metallic strip.

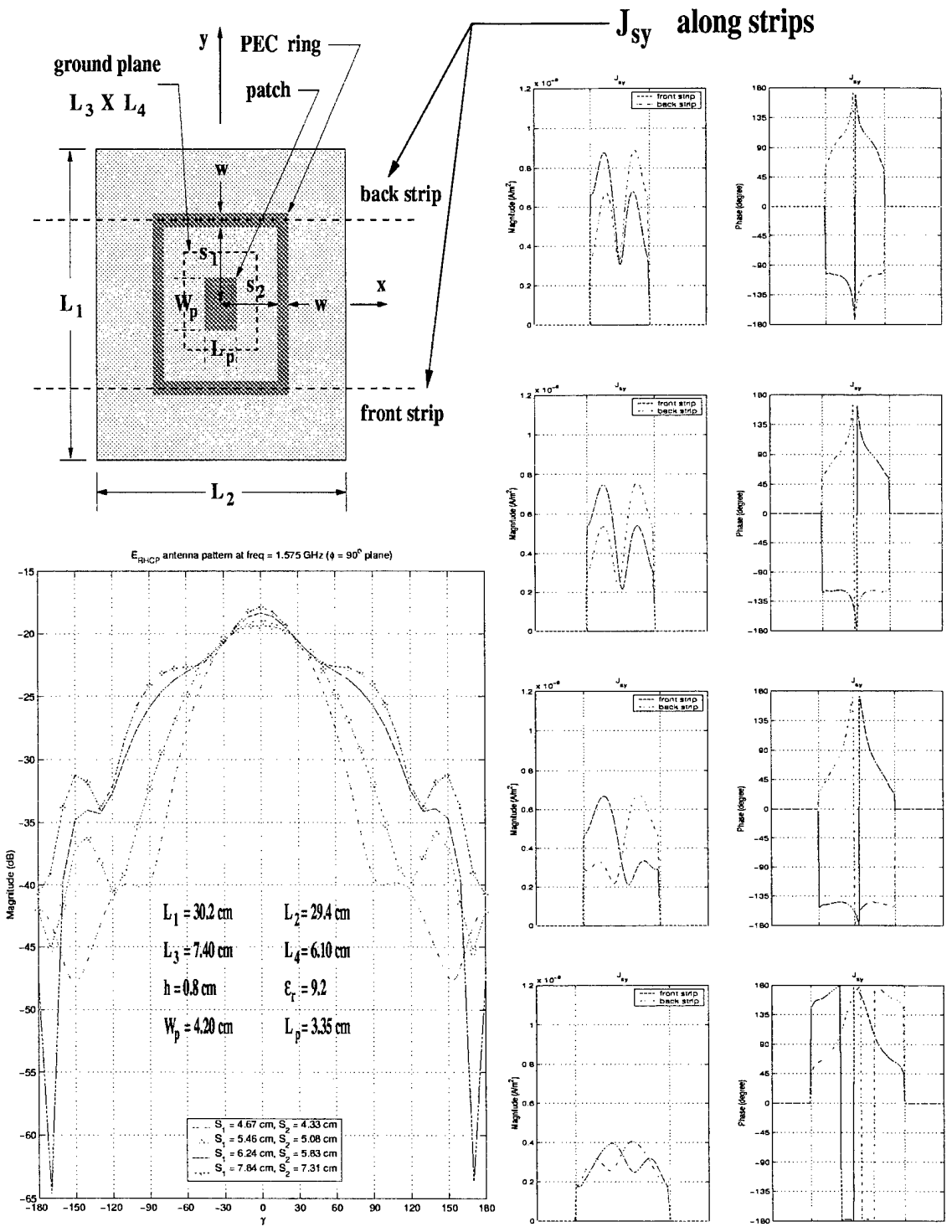

Figure 3.8: Induced surface current J_{sy} of the metallic ring with $h = 0.8$ cm and for different ring dimensions.

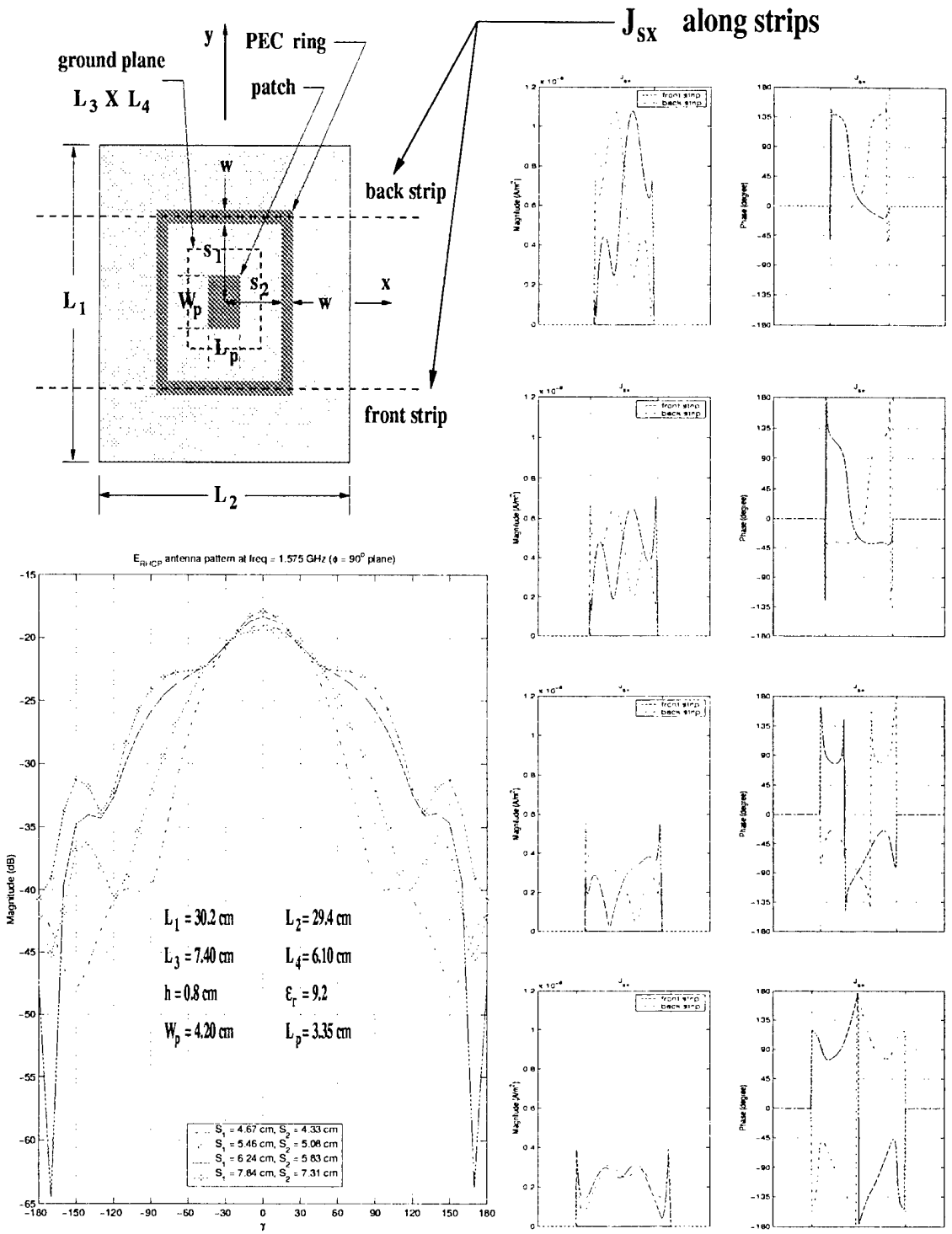

Figure 3.9: Induced surface current J_{sx} of the metallic ring with $h = 0.8$ cm and different ring dimensions.

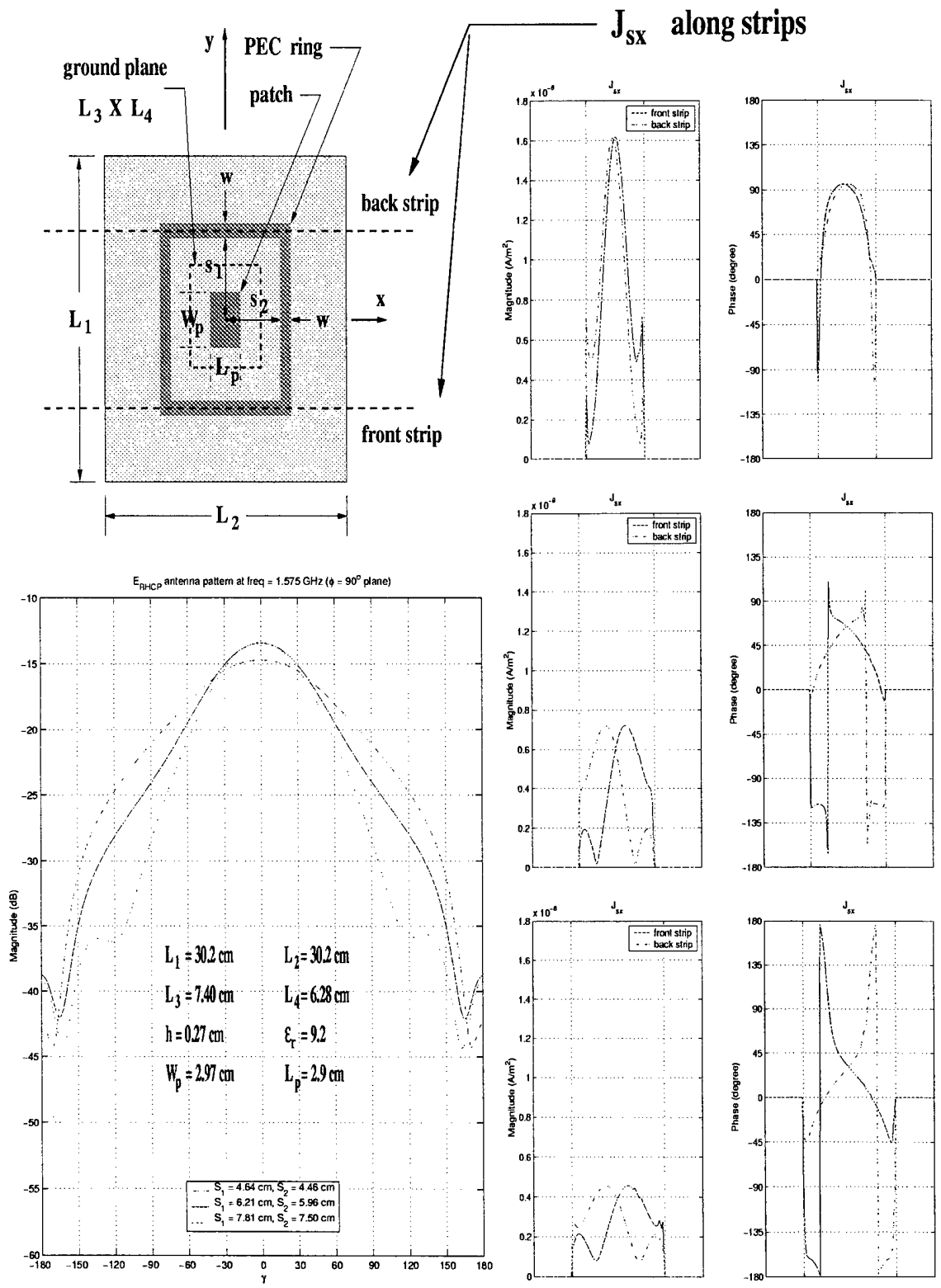

Figure 3.10: Induced surface current J_{sx} of the metallic ring with $h = 0.27$ cm and different ring dimensions.

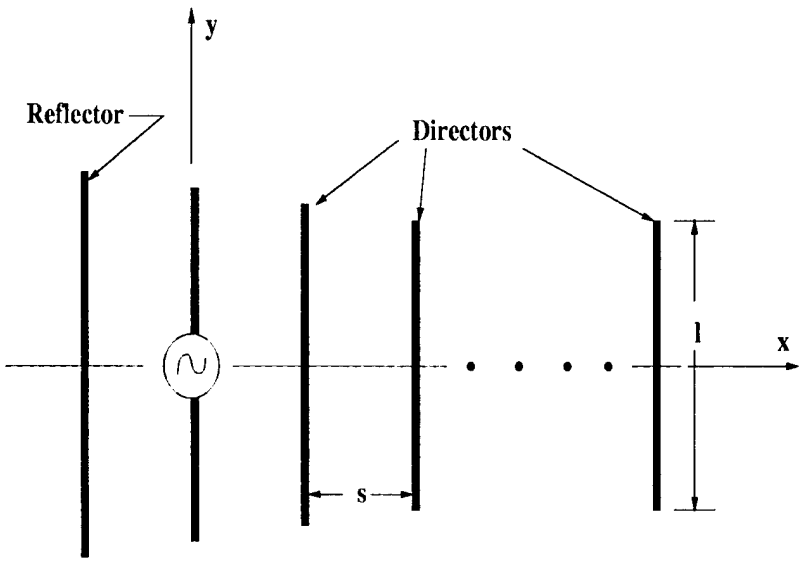

Figure 3.11: Yagi-Uda array configuration.

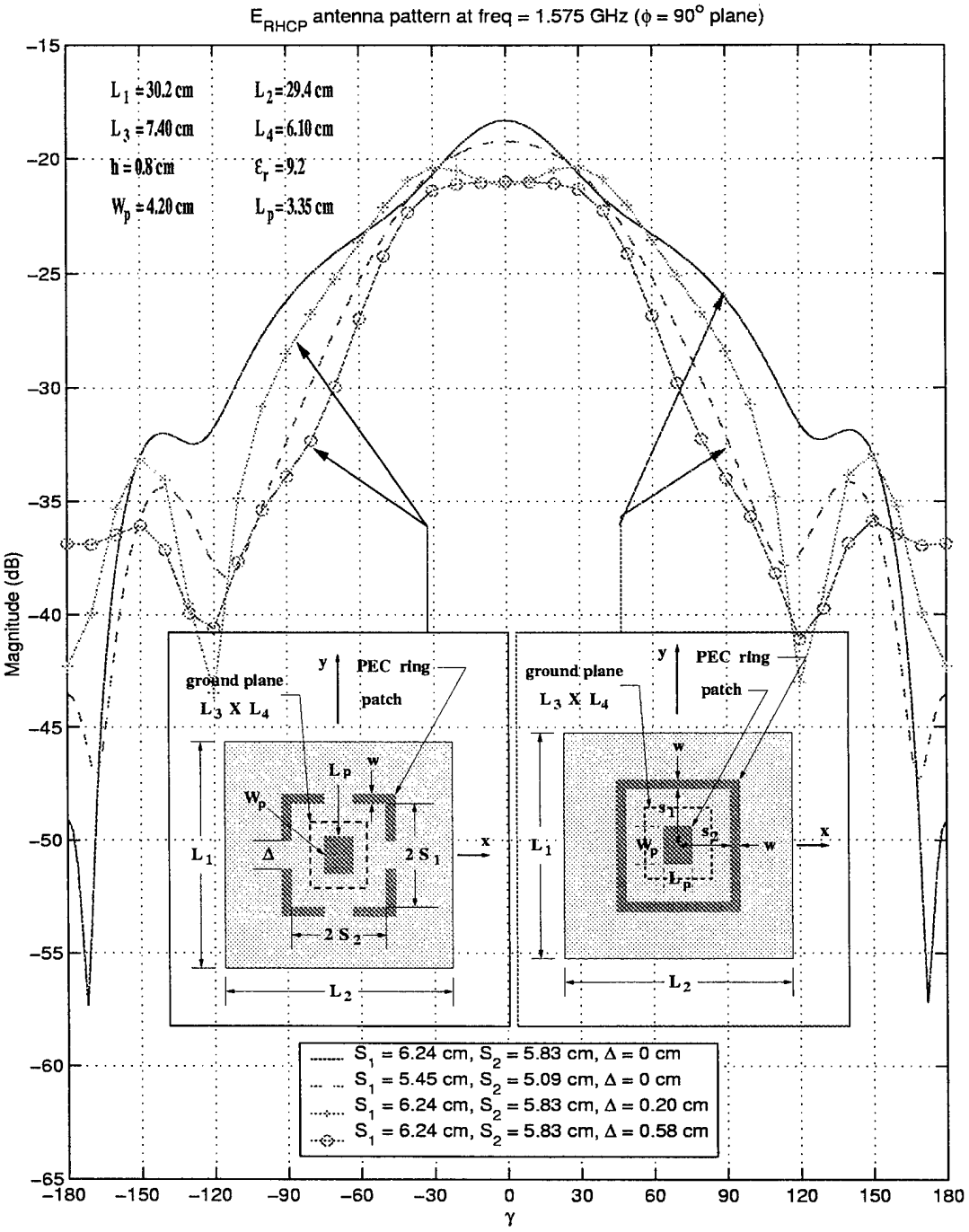

Figure 3.12: Calculated E_{RHCP} pattern of the reconfigurable antenna with capacitive loading.

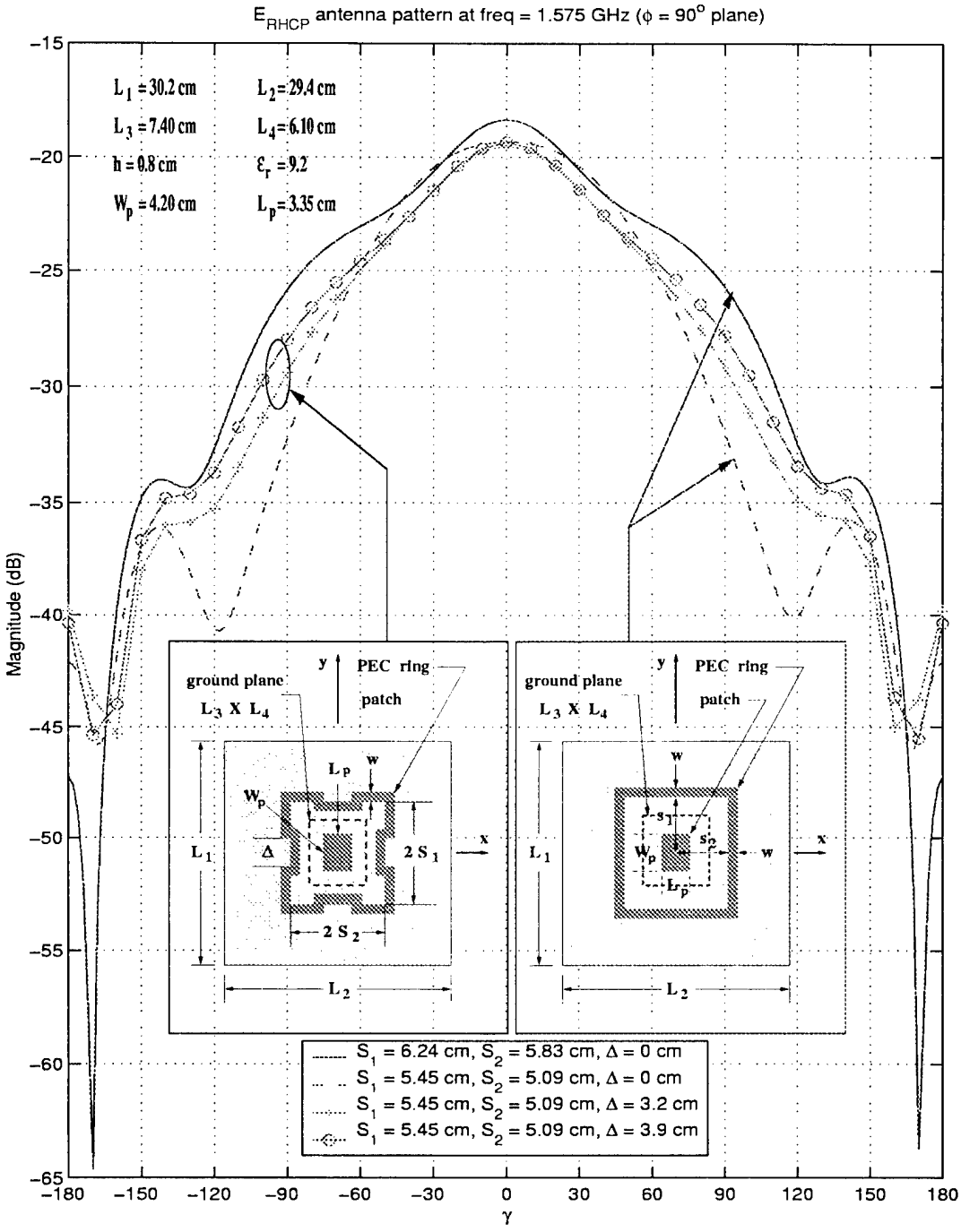

Figure 3.13: Calculated E_{RHCP} pattern of the reconfigurable antenna with inductive loading.

Chapter 4

FDTD Improvements

The design of a GPS antenna requires an accurate computational tool. The two parameters we need to calculate are the input impedance and the radiation pattern. Accurate input impedance calculations are difficult to achieve because of the need for accurate near-fields. The radiation pattern calculation of microstrip antennas with thin slots is also difficult. Thin slots are introduced to reduce the size of the patch; however, the field behavior in a thin slot is complicated. Accurate computation of these fields is required to achieve good results, especially in terms of polarization of the far-zone fields.

4.1 Input Impedance

One of the most popular configurations to feed a microstrip antenna is a coaxial probe. The inner conductor of the coaxial feeding line is attached to the radiating patch while the outer conductor is connected to the ground plane. The main advantage of this feeding technique is that fabrication and matching are quiet easy, and it has low spurious radiation [8]. On the other hand, it has a narrow bandwidth and it is difficult to precisely model the field in the neighborhood of the probe, especially for thick dielectric substrates. To improve the input impedance calculation, it is important to properly model these fields.

To understand the improved model for the fields near the probe, consider a thin wire and a contour path adjacent to a FDTD cell as illustrated in Figure 4.1 The thin wire in this case is much smaller than the FDTD cell. Normally the wire radius must

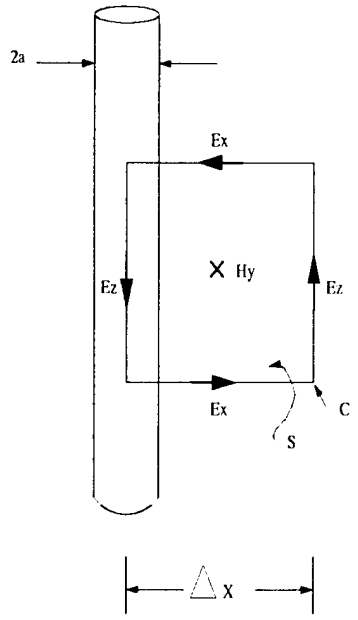

Figure 4.1: Faraday's law contour path for the thin wire FDTD modification

be less than half of the FDTD cell size. To account for the wire radius, the near field behavior dictated by Faraday's law is summarized in the following assumptions. First the scattered azimuthal magnetic field components and the scattered radial electric field components are assumed to vary as $1/r$ near the wire, where r is the distance from the wire center [15]. This type of static-field singularity is valid for $r < \lambda_o/10$. Furthermore, to maintain a reasonable spatial resolution, the grid size must be less than 0.1 wavelength. Moreover, the total E_z and H_y fields are evaluated at the z midpoint of the contour, and are assumed to represent the average values of their respective fields over the entire z interval [15].

In order to verify the improvement of the modification, we should compare the computed input impedance with measured input impedance results [16]. Figure 4.2 shows the comparison between the input impedance of an electrically thick rectangular microstrip antenna before and after the code modification, and the measured input impedance as well. As can be seen, the resistance from the modified FDTD calculation matches the measured resistance quite well. However, the reactance is shifted from the measured reactance by approximately 80 ohms, but still has almost the same shape. Clearly, the real part of the input impedance from the modified FDTD code

is in closer agreement with the measured data. Hence, the new probe fed model yields better results in terms of input impedance (real part) computation. However, a discrepancy in the reactance remains. Note that we do not have information about the radius of the probe for the measured data. We are using a value of a=0.2 mm for our calculated results. Keeping in mind that the reactance is more sensitive to the radius of the probe may explain the discrepancy in the reactance but not in the resistance.

It is interesting to note that the discrepancy between the calculated (modified FDTD) and measured reactances is approximately equal to the reactance of the probe. This is shown in Figure 4.3 where the calculated result is obtained by subtracting the probe reactance. We will continue to investigate this issue.

4.2 Narrow Slot model

The main motivation for introducing the narrow slot model in our FDTD code is to be able to analyze a microstrip antenna with a complicated geometry that involves narrow slots. When the slots are very narrow, the grid size becomes very small if we want to model the field within the slot accurately. However, using small grids will result in a very large problem that is time consuming. We will modify the FDTD algorithm so we can still use grids that are larger than the slot width without having an effect on the accuracy of our computations. Another goal is to improve the field computation near the edge of the conducting surfaces.

To accomplish these goals we first need to develop modifications for the configurations shown in Figure 4.4. This figure illustrates Faraday's law contour paths C1 through C12 used to derive FDTD algorithms for the normal magnetic field component, H_z [17]. For each Faraday's law contour path, the following assumptions concerning the near field physics are used to predict the field behavior near the edge of a conducting surface. First, the normal magnetic field component H_z evaluated in the middle of the grid is assumed to represent the average value of the magnetic field over the entire free space portion, and also has no variation in the x and y directions. Moreover, the electric field E_x is evaluated at the midpoint of each x-directed portion

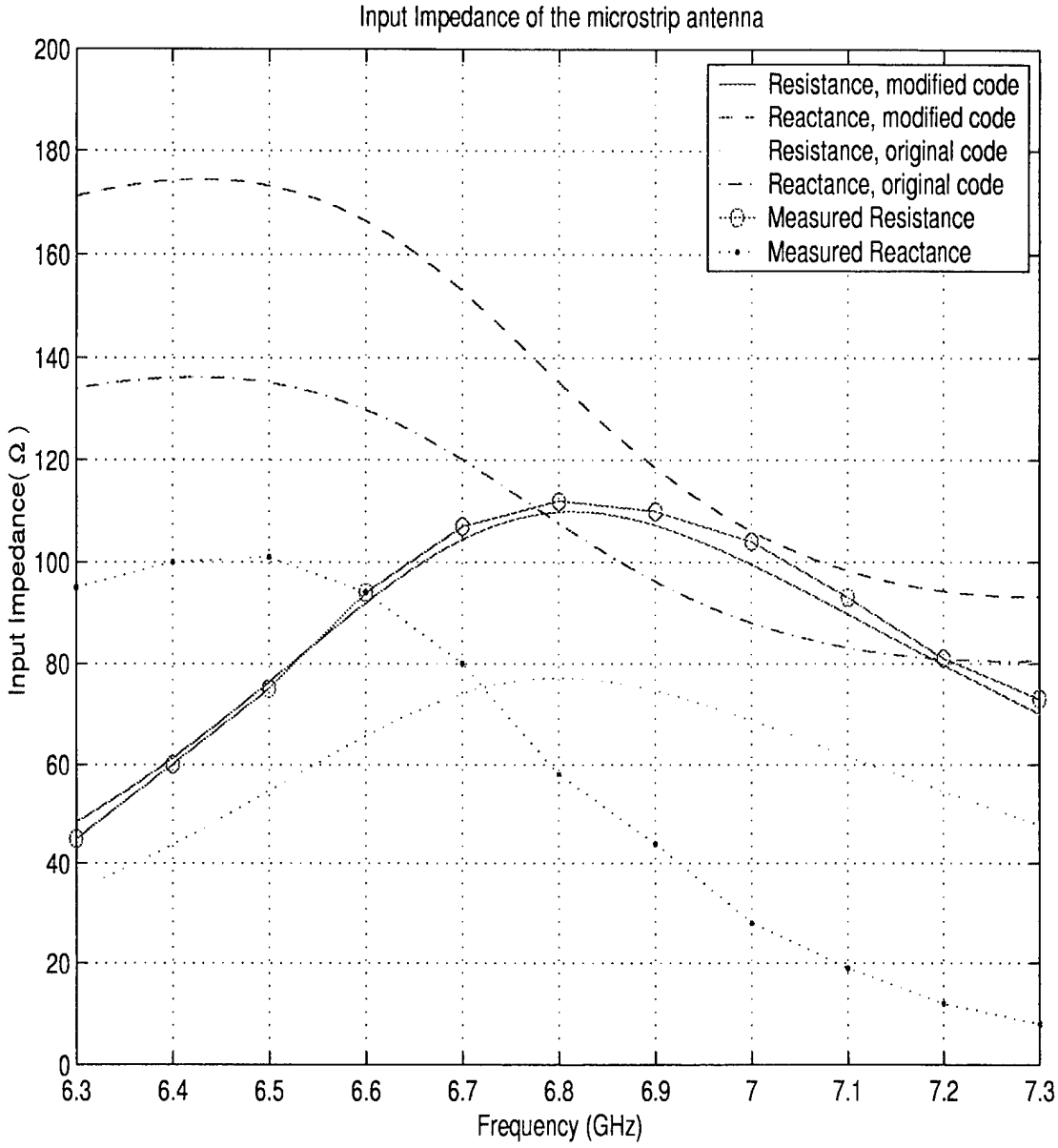

Figure 4.2: Input impedance comparison between FDTD computation and measured result of microstrip antenna

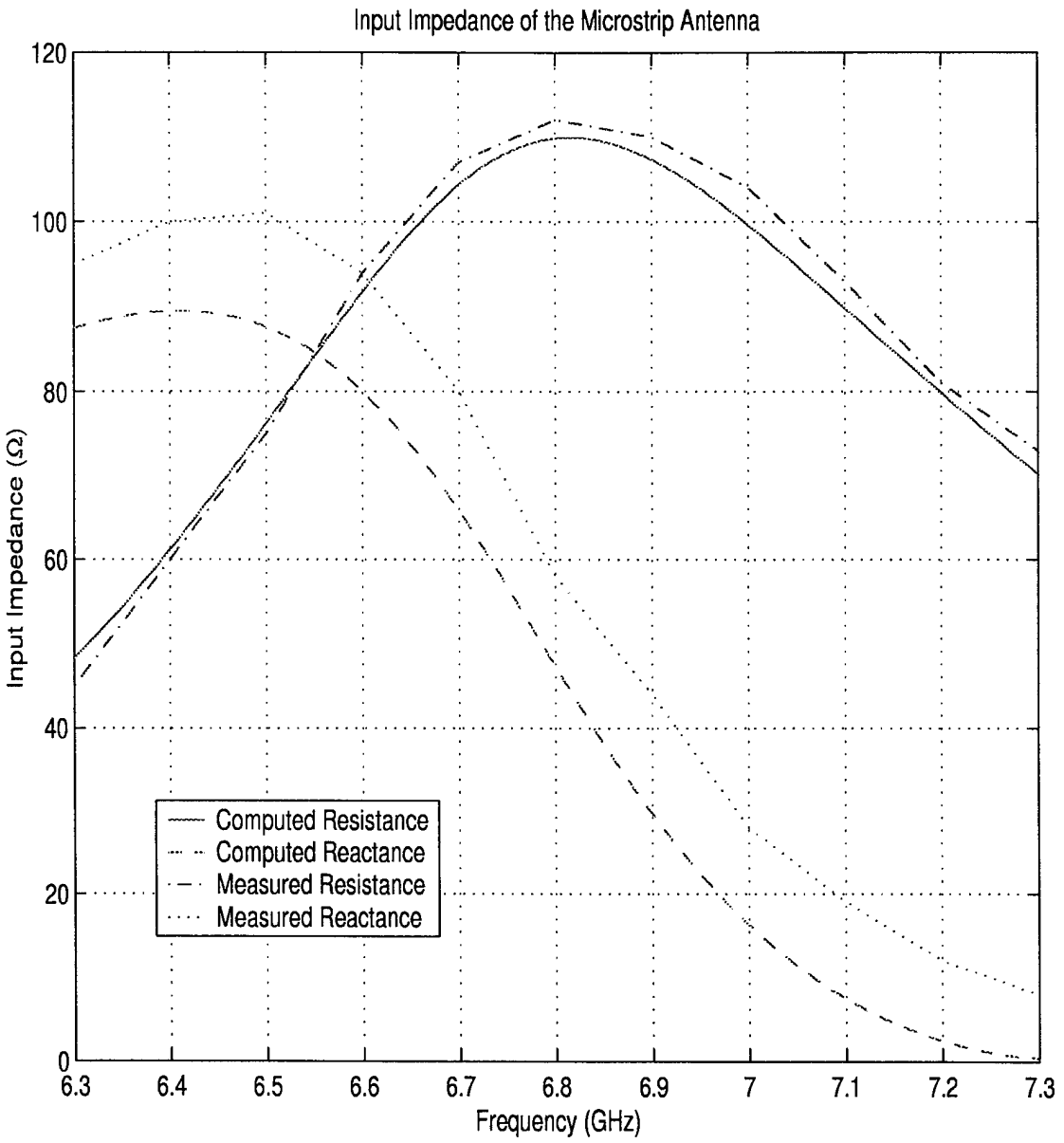

Figure 4.3: Input impedance comparison between modified FDTD code and measured result of microstrip antenna

of the contour, and assumed to represent the average value over the full x interval. Likewise, the electric field E_y is evaluated in the same fashion along the y-directed portion of the contour. We extended the above modifications to the case when the slot width is smaller than the FDTD grid size. We employed another set of Faraday's law contour paths as shown in Figure 4.5 to obtain a smaller computational domain size. The field behavior assumptions are still the same as in the previous (Figure 4.4) geometry.

Figures 4.6 and 4.7 illustrate the field pattern from two computations; unmodified and modified (thin slot case) FDTD code. We are using a square patch microstrip antenna with a slit on the radiating patch. The square patch has a length of 39.7 mm(L), and is printed on a substrate of thickness 1.6 mm(h) with a relative permittivity of 4.4. To achieve a radiated field with circular polarization, the slit width is set to 1 mm, and the slit length is adjusted to be 6 mm [18]. The feeding point is at C as illustrated in Figure 4.6. Note that when using the modified code, we can use larger grids than when using the unmodified code. This results in a smaller computational domain and shorter time to achieve convergence. In these examples the grid size for the modified code is 2.4 times larger than the grid of the unmodified code. As can be seen from these figures, both RHCP radiation patterns match each other in the main beam region as well as the measured pattern (not shown in these figures). However, the agreement in the region beyond the main beam is not as good. The LHCP patterns agree reasonably well in the main beam, but there is substantial disagreement away from this region, especially in the H-plane. It appears that the thin-slot modification has an important effect in the region away from the main beam. Although not shown here, the agreement between the measured and calculated LHCP (cross-polarized component) patterns is not good, even in the main beam. We continue to investigate the reasons for this disagreement.

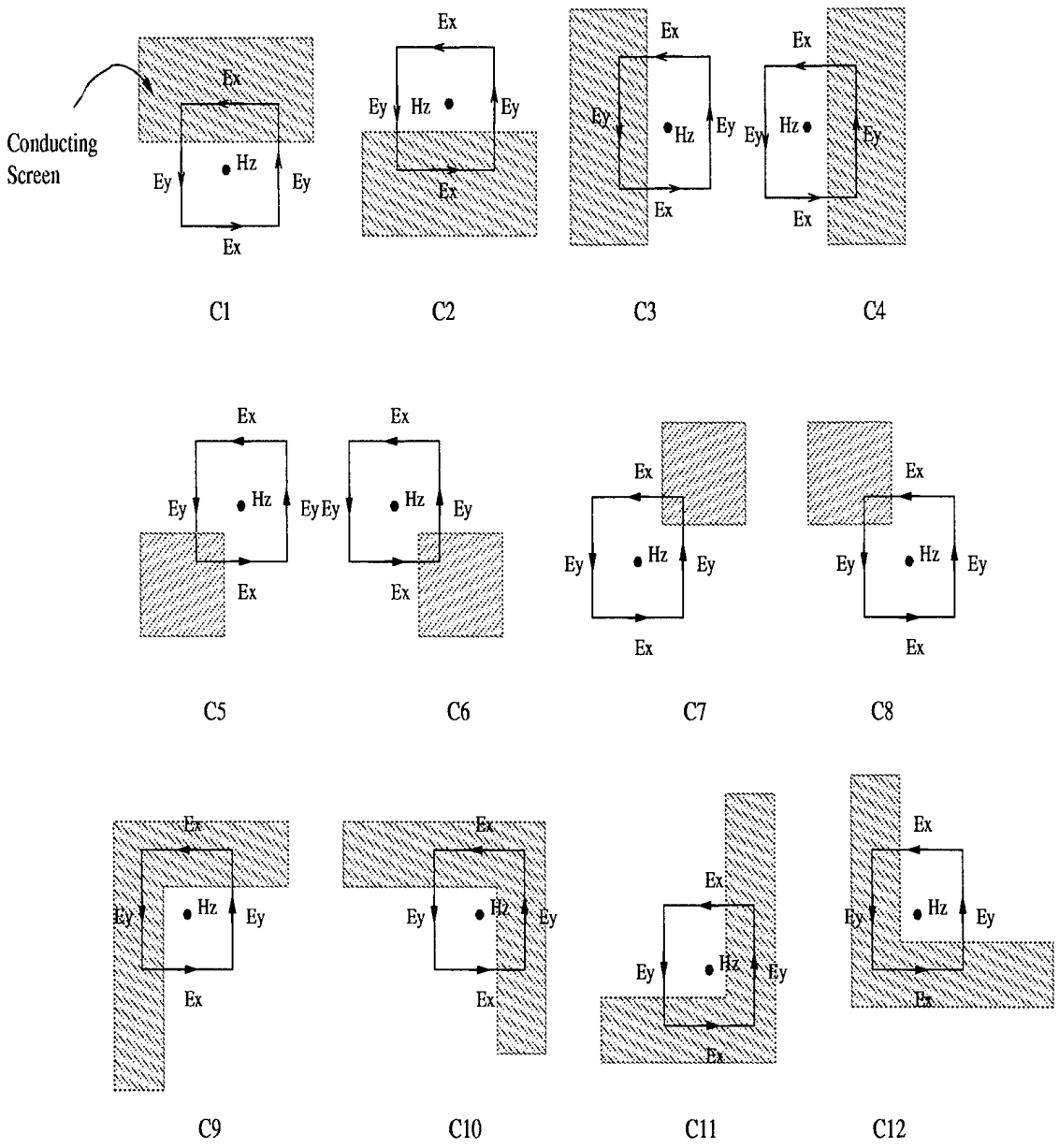

Figure 4.4: Faraday's law contour paths for 12 different two-dimensional planar conducting screen cases

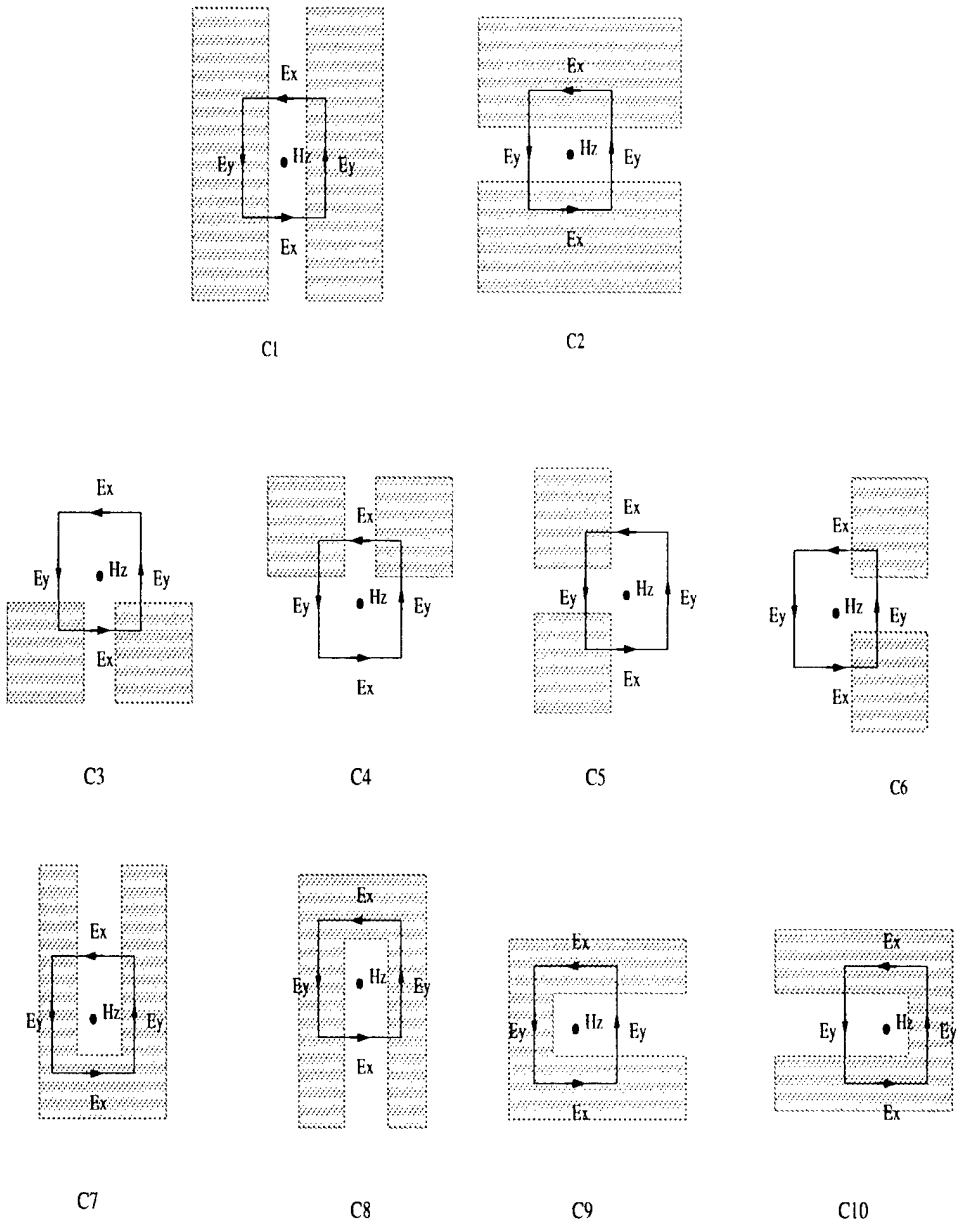

Figure 4.5: Faraday's law contour paths for 10 different two-dimensional planar conducting screen cases where the slot width is smaller than the grid size

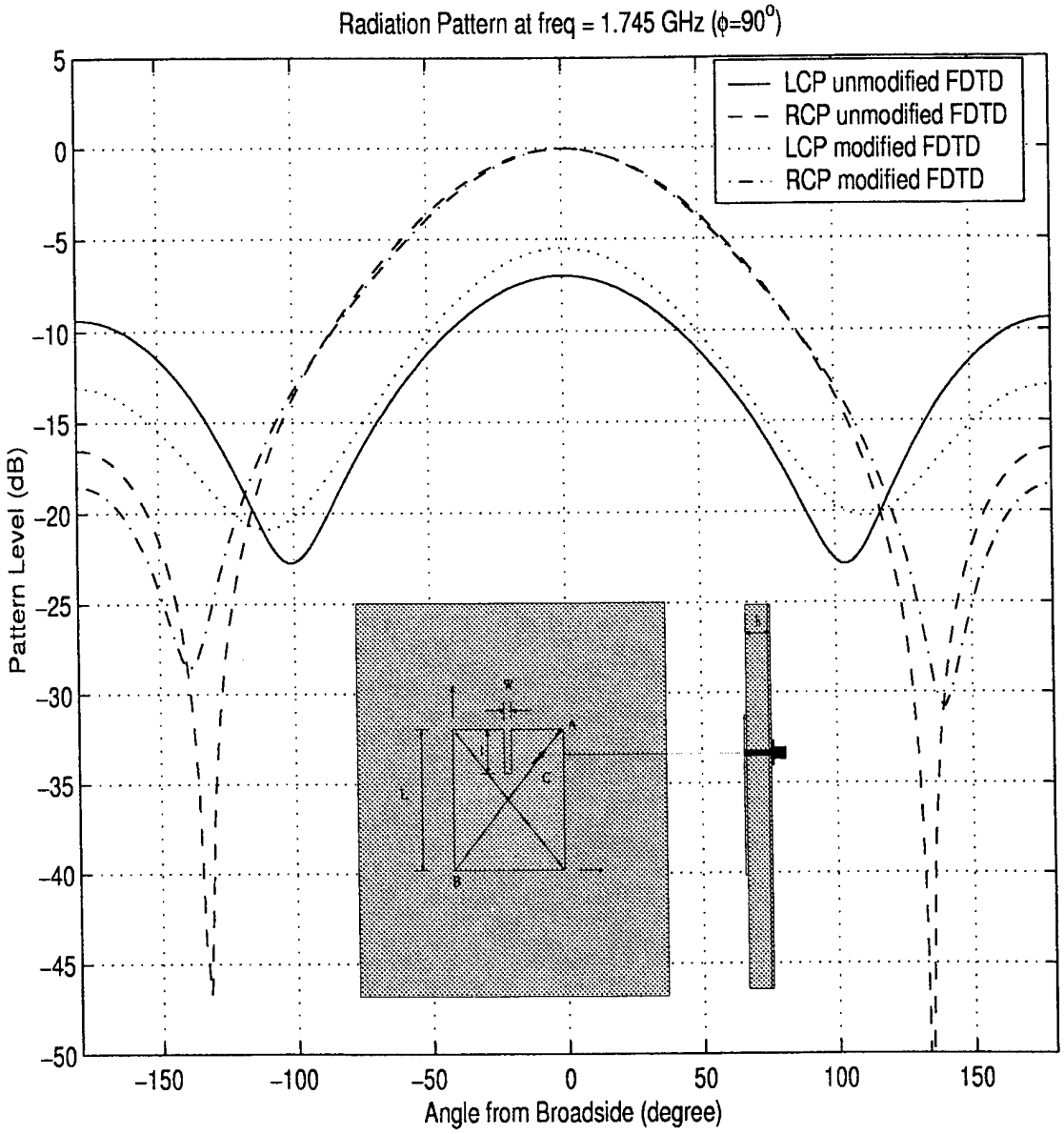

Figure 4.6: E-plane field patterns of a single-feed circularly polarized microstrip antenna with a slit

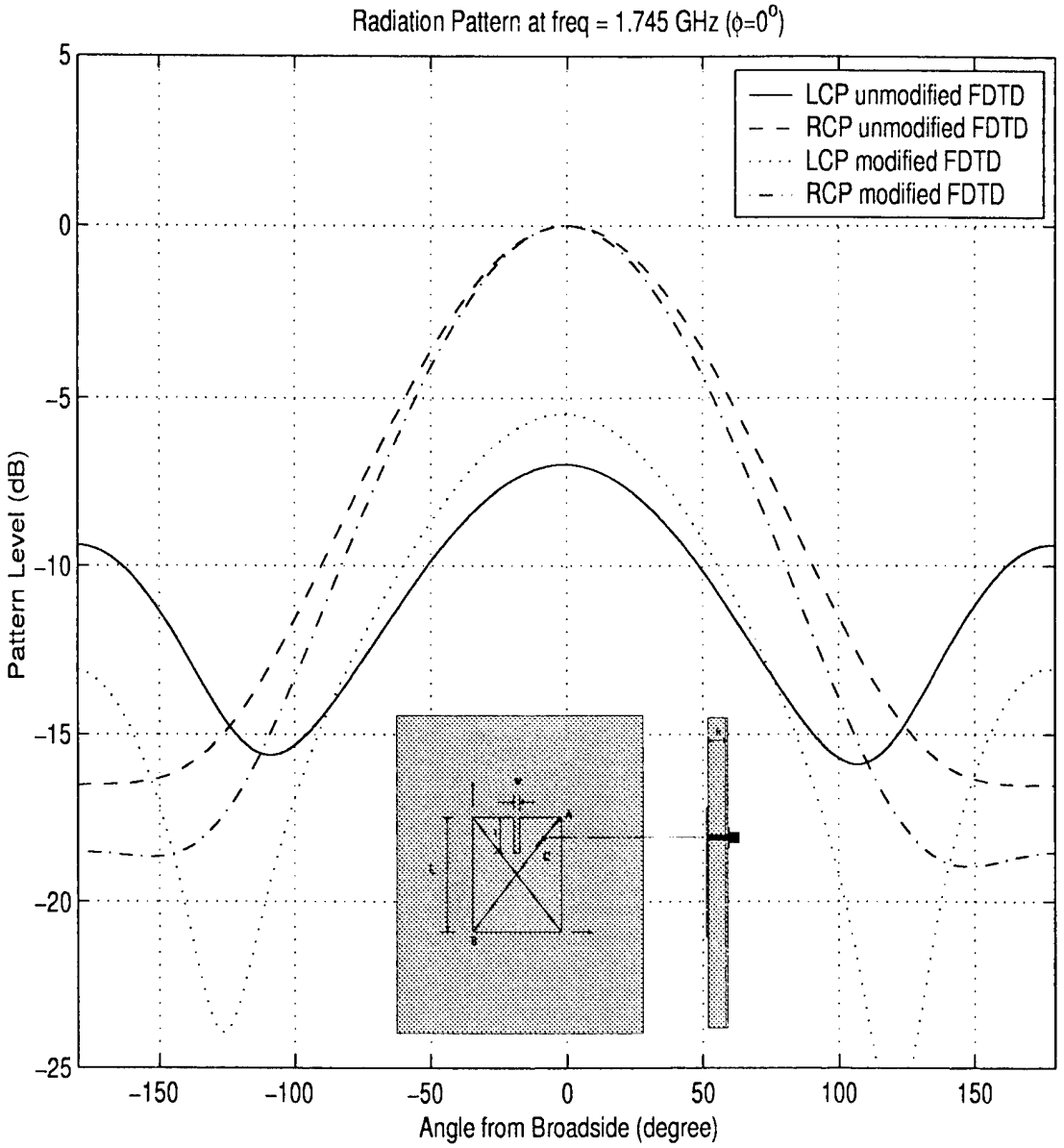

Figure 4.7: H-plane field patterns of a single-feed circularly polarized microstrip antenna with a slit

Chapter 5

Antenna Performance in Presence of Jamming signals

Jamming signals have been identified as a serious threat to GPS receiving systems in hostile environments. A reconfigurable GPS antenna has been proposed as a technique for mitigating the effect of jamming signals at the receiving site. In previous studies [5, 6, 19], a scheme for controlling the radiation pattern of circularly polarized (CP) microstrip antennas was presented. Two designs were developed for a CP antenna. Both designs (referred to as Designs I and II) have a metallic ring; however, Design I (see Figure 1.3 in [6]) has a larger and wider ring than the other. It also has a ground plane that is larger than the ring, usually the same size as the substrate. Furthermore, the design with the smaller ring (Design II) has a ground plane that is smaller than the ring (see Figure 1.1). The overall size of Design I is larger than Design II. However, Design I, due to its wider ring, appears to be more effective in modifying the pattern beamwidth for the vertically polarized field component. Keeping in mind that we are assuming that jamming signals are vertically polarized, we will use design I for our simulations. We are currently working in Design II so it can be effective in modifying both polarizations, namely, vertical and horizontal.

Design I consists of a microstrip antenna with an array of diode-loaded metallic strips as shown in Figure 5.1. In this chapter, an study of the jamming signal suppression performance and the coverage of the adaptive antenna will be carried out. However the circularly polarized antenna without any parasitic ring will be

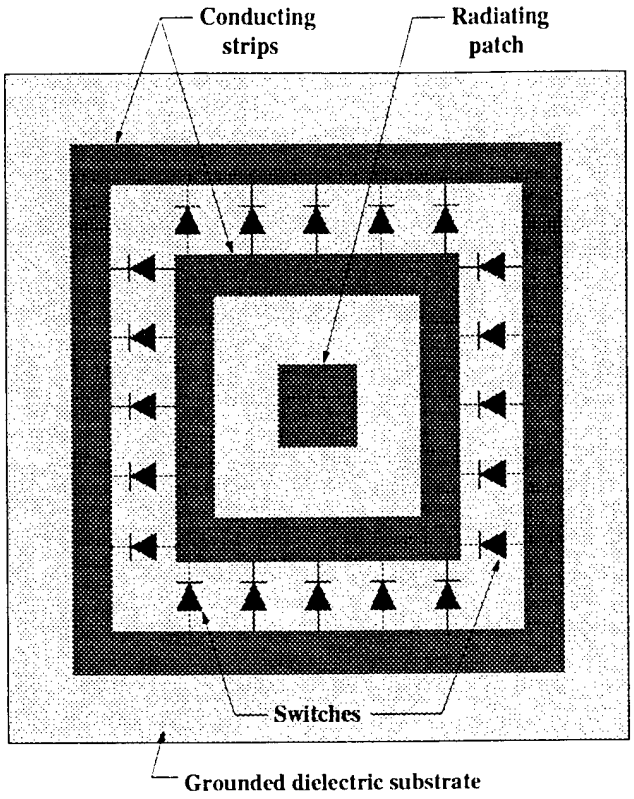

Figure 5.1: Design I: Circularly polarized microstrip antenna with an array of diode-loaded metallic strips (top view). Note that ground plane is larger than the ring. In this case the ground plane is the same size as the substrate

also included in the performance investigation. The following figures illustrate three configurations of the antenna being used in this performance investigation.

Figure 5.2 shows a top view of the circularly polarized microstrip antenna without any metallic ring and Figure 5.3 depicts the circularly polarized microstrip antenna with a large parasitic metallic ring (diodes in Figure 5.1 are on). Finally, Figure 5.4 illustrates the circularly polarized microstrip antenna with two small parasitic metallic rings (diodes in Figure 5.1 are off).

Although our study has been centered on the development of a reconfigurable GPS printed antenna, this antenna will be mounted on an aircraft. This implies that its radiation pattern will be altered by the structure on which is mounted. If we are going to study the performance of the antenna in the presence of jamming signals, we need to model the structure on which it is mounted. If the antenna is

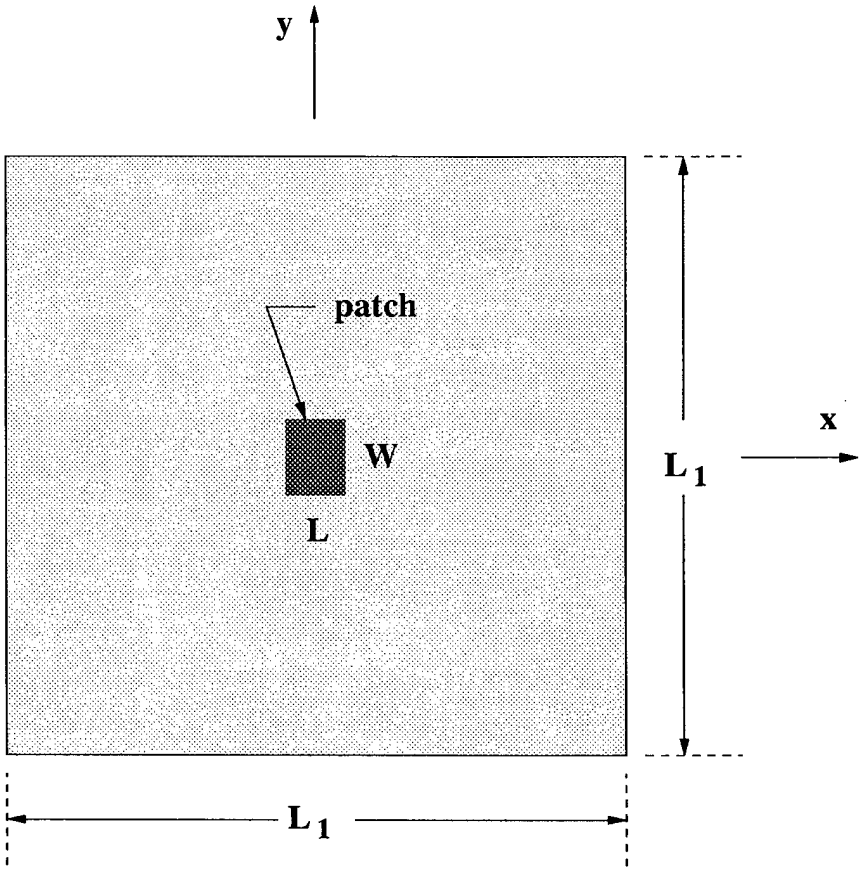

L=3.76 cm , W = 2.41 cm, L_1 =35.19 cm

Figure 5.2: Circularly polarized microstrip antenna without a metallic ring (top view)

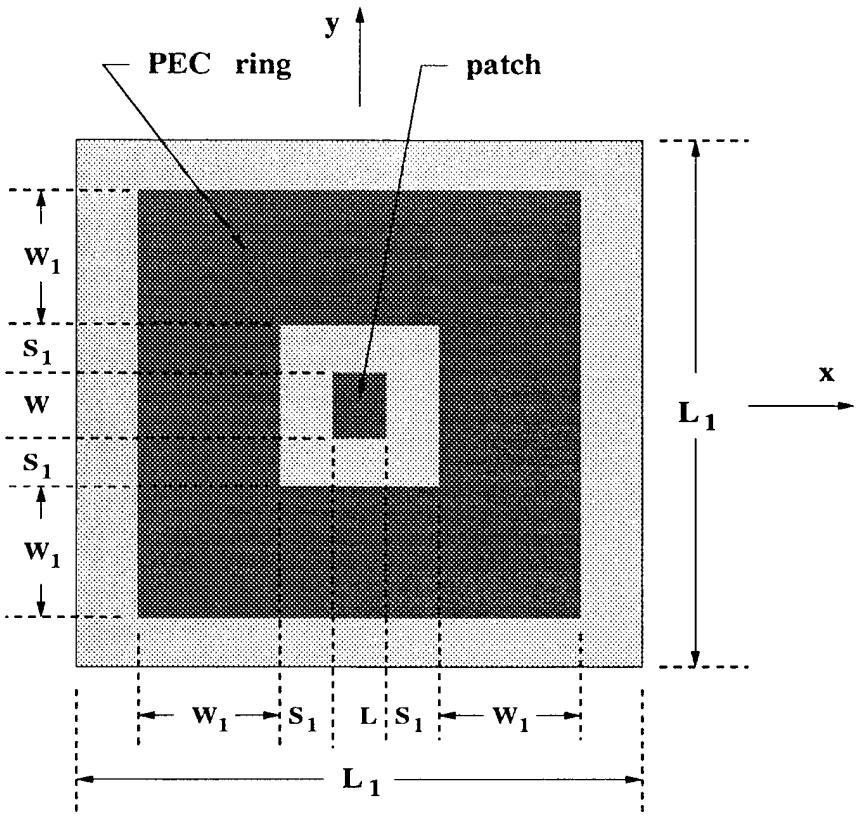

L =3.76 cm, W = 2.41 cm, L_1 = 35.19 cm

W_1=7.94 cm, S_1=3.35 cm

Figure 5.3: Circularly polarized microstrip antenna with one metallic ring (diode on)

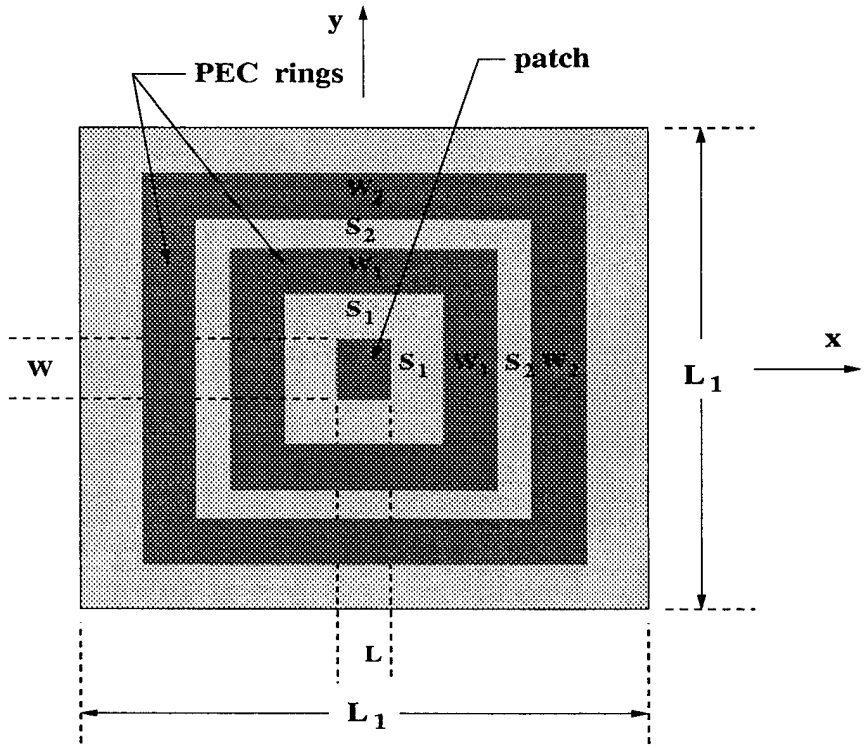

L = 3.76 cm, W = 2.41 cm, L_1 = 35.19 cm

S_1= 3.35 cm, W_1 = 2.58 cm

S_2= 3.16 cm, W_2 = 2.20 cm

Figure 5.4: Circularly polarized microstrip antenna with two metallic rings (diode off)

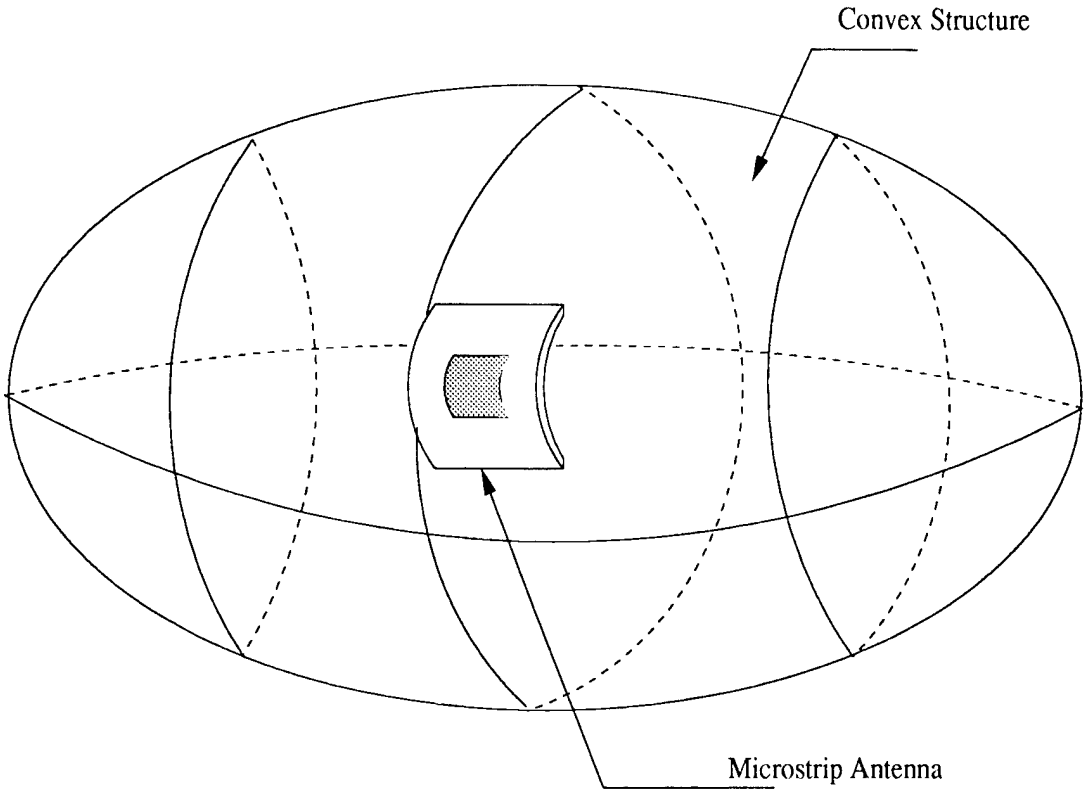

Figure 5.5: Antenna mounted on convex surface

assumed to be mounted on the fuselage of an aircraft, the fuselage can be modeled by a convex structure as depicted in Figure 5.5 where other structures of the aircraft have been neglected. As mentioned above, the net effect of the structure will be to change the radiation pattern, especially along and below the horizon where surface effects are important. The radiation pattern of the antenna mounted on the fuselage of an aircraft will be calculated in future studies. At the present time, the antenna is assumed to be mounted on an infinite planar ground plane as shown in Figure 5.6. This planar ground plane is a reasonable model of the fuselage (angles above the horizon) when the radius of curvature of the fuselage is large in terms of wavelength.

The following radiation patterns demonstrate the feasibility of the adaptive scheme for the antenna mounted on an infinite planar ground plane. Figure 5.7 depicts the calculated RHCP, LHCP, phi and theta components of the radiation pattern in the $\theta = 0^0$, 30^o and 60^o plane cuts at L1 band. Furthermore Figures 5.8 shows the calculated RHCP, LHCP, phi and theta components of the radiation pattern in the

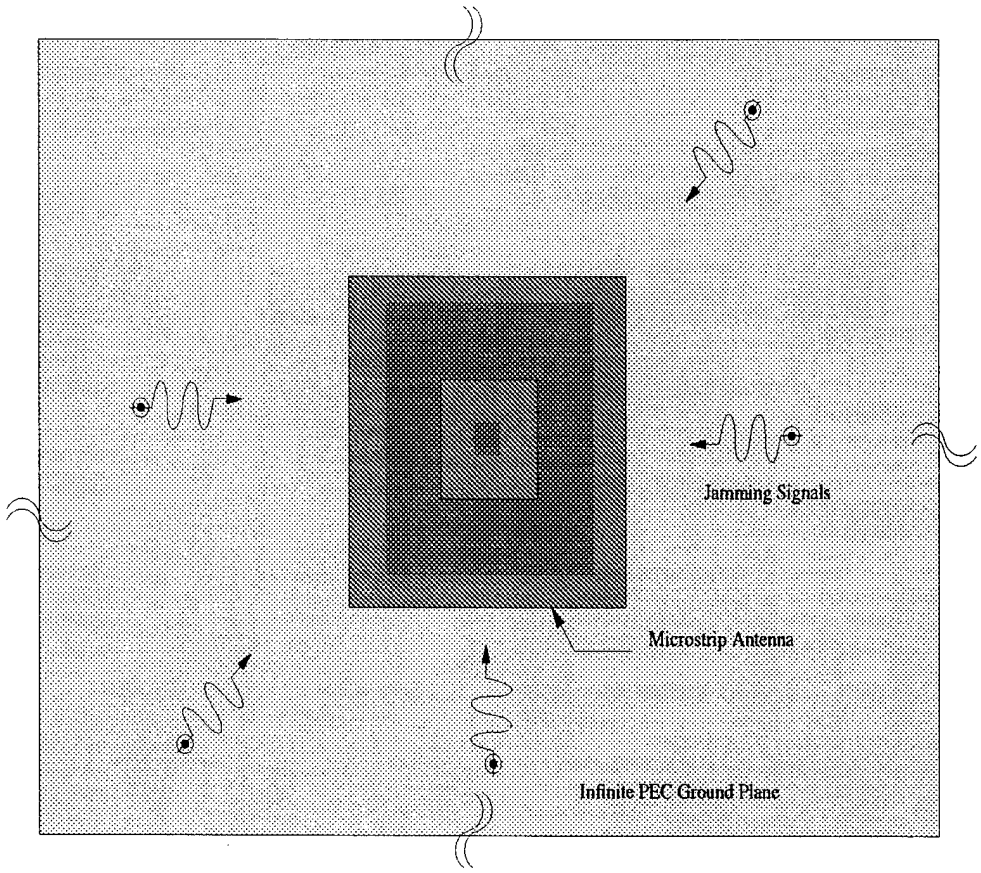

Figure 5.6: Reconfigurable antenna mounted on planar ground plane (top view). Jamming signals can be incident from any direction in azimuth

$\theta = 90^0$, 120^o and 150^o plane cuts also at L1 band. It can be observed from these figures that the antenna pattern is reconfigurable, especially in the end-fire direction. Noting that the direction of the incoming interfering signals is usually around the end-fire region, the effect of the jamming signals can be mitigated by selecting the radiation pattern which minimizes the gain in that direction.

As mentioned before, we will mainly be concerned with two antenna performance parameters, namely, jamming signal suppression and coverage. Note that these performance metrics are dependent on well known antenna parameters such as directivity, gain, beamwidth, front to back ratio, etc. Frequency bandwidth and group delay are also important; however, they are not considered in this report. First we will focus on how well the antenna suppresses interfering signals by using the adaptive scheme. The second task is to study the antenna coverage as a function of antenna gain. The configuration of the system setup is explained in the following section.

5.1 System Configuration

The purpose of this study is to demonstrate how the reconfigurable printed antenna reduces the effect of the jamming signals. Figure 5.6 shows a top view of a scenario of the antenna performance experiment. The antenna is mounted on a planar infinite ground plane. The vertically polarized jamming signals can arrive to the antenna from an arbitrary direction in azimuth. However, their elevation incident angles are restricted to 0^o to 10^o as shown in Figure 5.9. The operating frequency is 1.575 GHz which corresponds to the L1 band. By employing the Friis transmission equation, the jamming power received by the antenna is determined by

$$P_r = \left(\frac{\lambda}{4\pi R}\right)^2 (1 - |\Gamma_t|^2)(1 - |\Gamma_r|^2) G_t(\theta, \phi) G_r(\theta, \phi) PLF(\theta, \phi) P_t \qquad (5.1)$$

where P_r and P_t are the power of the jamming signal received by the reconfigurable antenna and the transmitted power from the jamming source, respectively. R is the distance between the jamming source and the receiving antenna, while Γ_t and Γ_r are the reflection coefficients of the transmitting and receiving antennas, respectively.

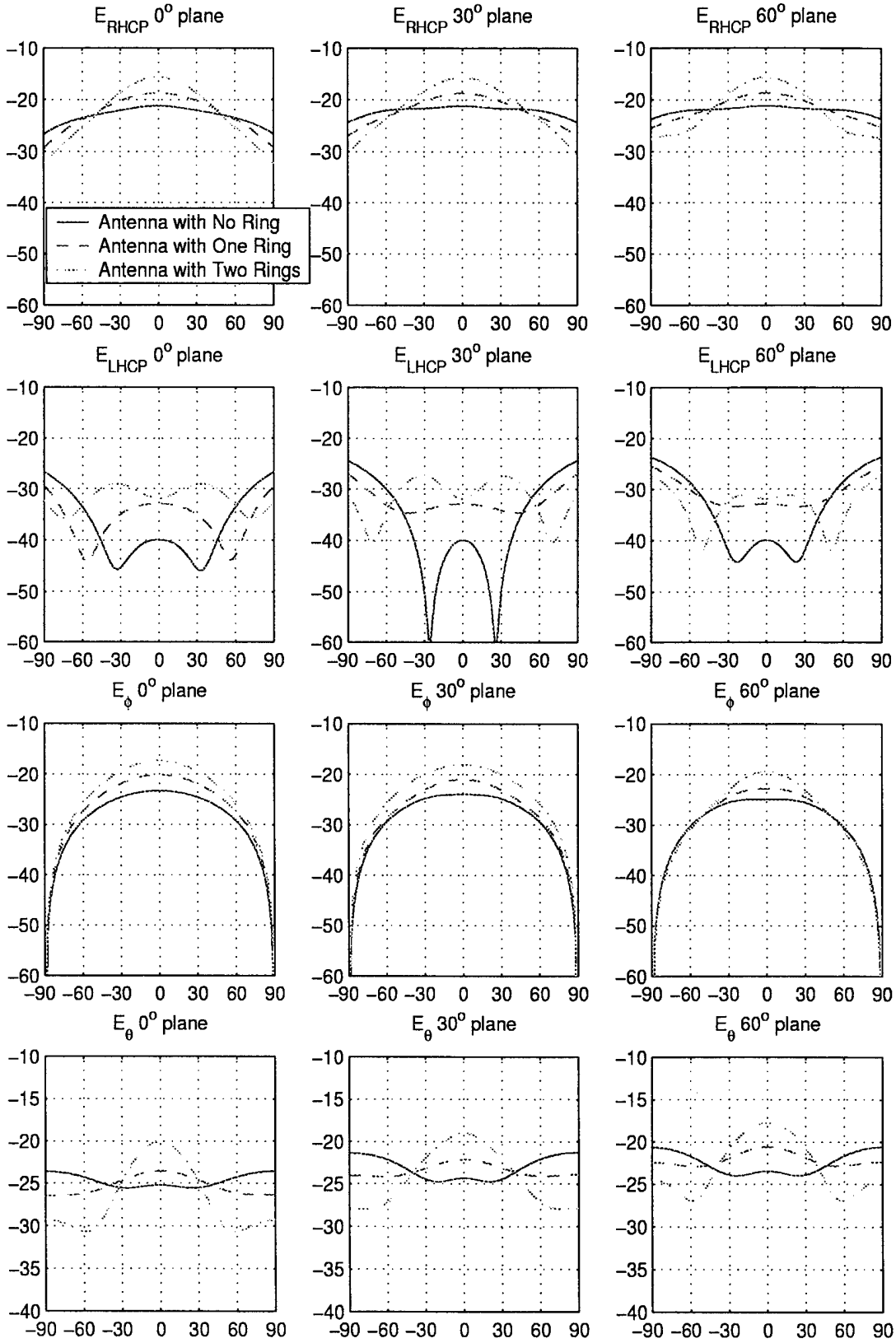

Figure 5.7: Radiation patterns of reconfigurable antenna in 0^o, 30^o and 60^o plane cuts, L1 band

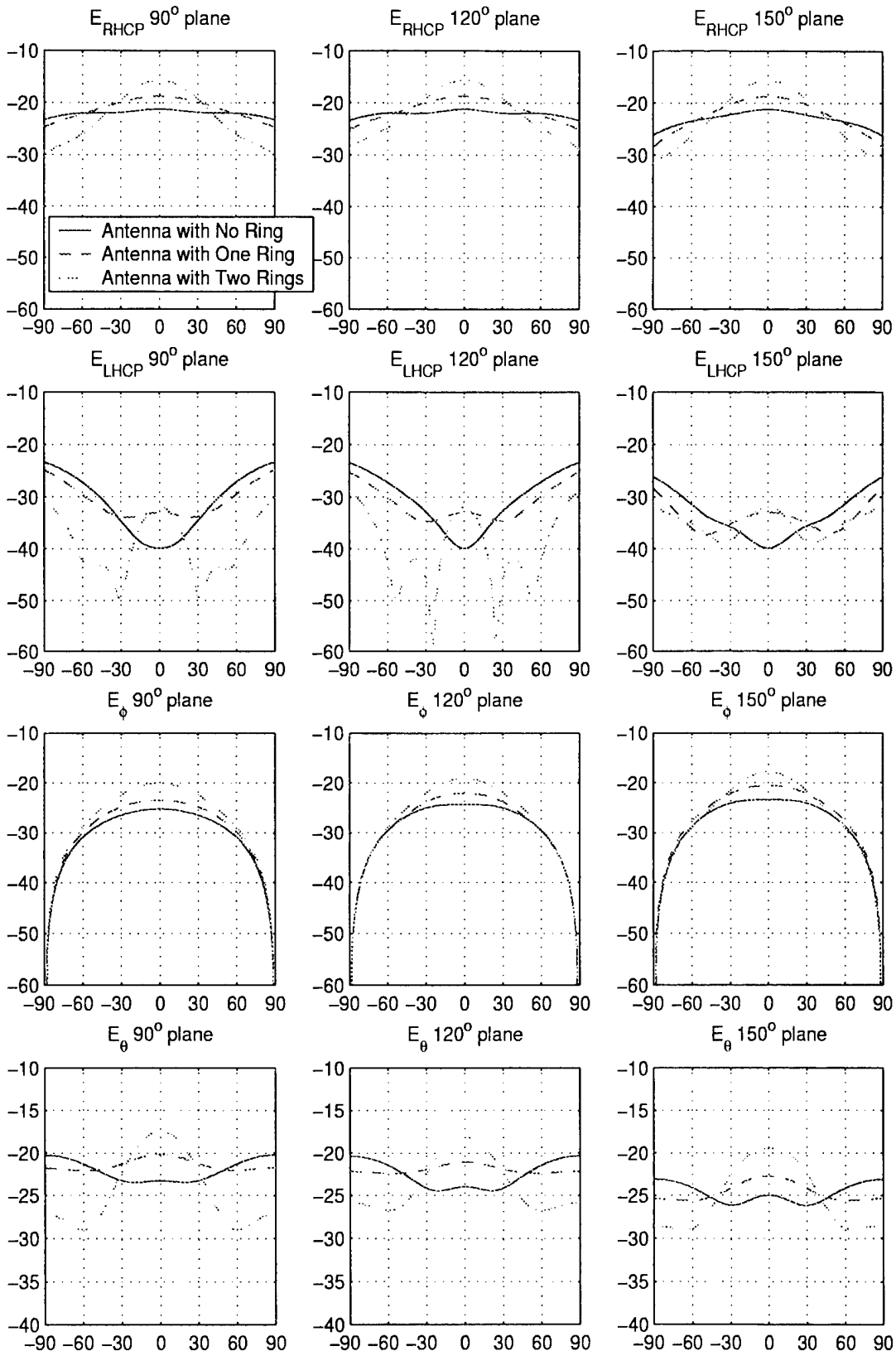

Figure 5.8: Radiation patterns of reconfigurable antenna in $90^o, 120^o$ and 150^o plane cuts, L1 band

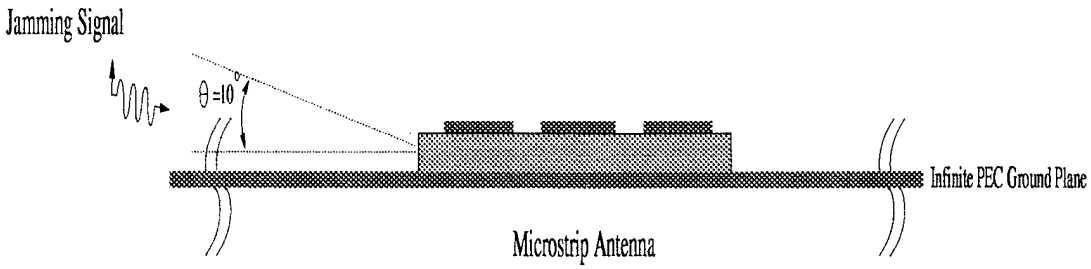

Figure 5.9: An scenario for reconfigurable antenna performance test (side view)

Similarly, G_t and G_r are the gain of the transmitter and the reconfigurable antenna, respectively. Finally, PLF is the polarization loss factor between the jamming signal and the receiving antenna.

Note that we assume that there is no reflection at the input port of the receiving antenna ($\Gamma_r = 0$) and also assume that $(\frac{\lambda}{4\pi R})^2(1 - |\Gamma_t|^2)G_t(\theta, \phi)P_t$ is approximately 50 dB. As a result, the above Friis transmission equation is simplified to

$$P_r = 50 + G_r(\theta, \phi) + PLF(\theta, \phi) \qquad \text{(dB)} \qquad (5.2)$$

Equation (5.2) is valid for a single jammer. However, in this study we are assuming that there are multiple jammers interfering with the antenna. Assuming that all the jamming signals are uncorrelated, the total received power is equal to the sum of the received power from each jammer, namely,

$$P_{rt}(N) = \sum_{i=1}^{N} 10^{\frac{P_{ri}(dB)}{10}} \qquad \text{(Watts)} \qquad (5.3)$$

$$P_{rt}(N) = 10 \log \sum_{i=1}^{N} 10^{\frac{P_{ri}(dB)}{10}} \qquad \text{(dB)} \qquad (5.4)$$

where P_{rt} is the total jamming power received from N jammers.

The numerical results in the next section were obtained as follows. The incident angles θ and ϕ were considered to be random variables with a uniform distribution. For each jamming source, the pair of angles (θ, ϕ) were calculated 100 times and the

received power calculated for each pair. An average power was obtained from these set of values. This process was repeated for each jammmer.

Coverage is the other aspect of antenna performance to be considered. Since the desired signals are received from GPS satellites, the domain of interest is assumed to be $0° \leq \theta \leq 80°$ in elevation and $0° \leq \phi \leq 360°$ in azimuth. Before we define coverage, we need to define a new parameter that is related to the gain of the antenna, but it also includes the polarization loss factor. This modified antenna gain (dB) is given by

$$\tilde{G}(dB) = G(db) + PLF(\theta, \phi) \tag{5.5}$$

The coverage as a function of $\tilde{G}$ is then defined as the ratio of two solid angles, namely,

$$Coverage(\tilde{G}) = 100\frac{\Omega(\tilde{G})}{\Omega_r} \tag{5.6}$$

where

$$\Omega_r = \int_0^{4\pi/9}\int_0^{2\pi} \sin\theta d\phi d\theta \approx 5.192 \qquad \text{(str.)} \tag{5.7}$$

and $\Omega(\tilde{G})$ is the solid angle where the modified gain of the antenna is larger than $\tilde{G}$.

5.2 Antenna Performance

In most of the results that follow, an ideal isotropic antenna is used as reference. This antenna is assumed to have a gain and PLF equal to zero dB everywhere. Figure 5.10 shows the received jamming power as a function of the number of jammers. As can be seen, the power received by the antenna without a parasitic ring has the worst performance (maximum received power) and is slightly different from the isotropic antenna case. This is expected since the pattern for this antenna is strong around the horizon. On the other hand, the radiation pattern of the microstrip antenna with two small rings (switches are off) minimizes the received power. Figure 5.11

demonstrates the difference in performance between the isotropic antenna and the reconfigurable antenna for three operating states. Obviously, the microstrip antenna with two parasitic rings (switches off) yields the most jamming signal suppression. It is also clearly seen that the antenna with a metallic ring performs better that the antenna without a parasitic ring. In addition, Figure 5.12 depicts the difference in performance among the three operating states of the reconfigurable antenna. It can be observed that the received power can be either decreased or increased from the reference (received power from the antenna with all diodes on). In our application, we definitely need to lower the jamming received power as much as possible, therefore the radiation pattern yielding the minimum received power will be chosen.

Coverage is the next aspect of antenna performance to be considered. Figure 5.13 represents the antenna coverage as a function of the modified antenna gain $\tilde{G}$ defined above. It is clearly seen that the coverage is inversely proportional to the antenna gain. This suggest that a good performance in terms of coverage and suppression of jamming power requires some trade offs. A high gain GPS antenna will have a narrow beamwidth and good jamming power suppression capabilities. However, its coverage will not be good.

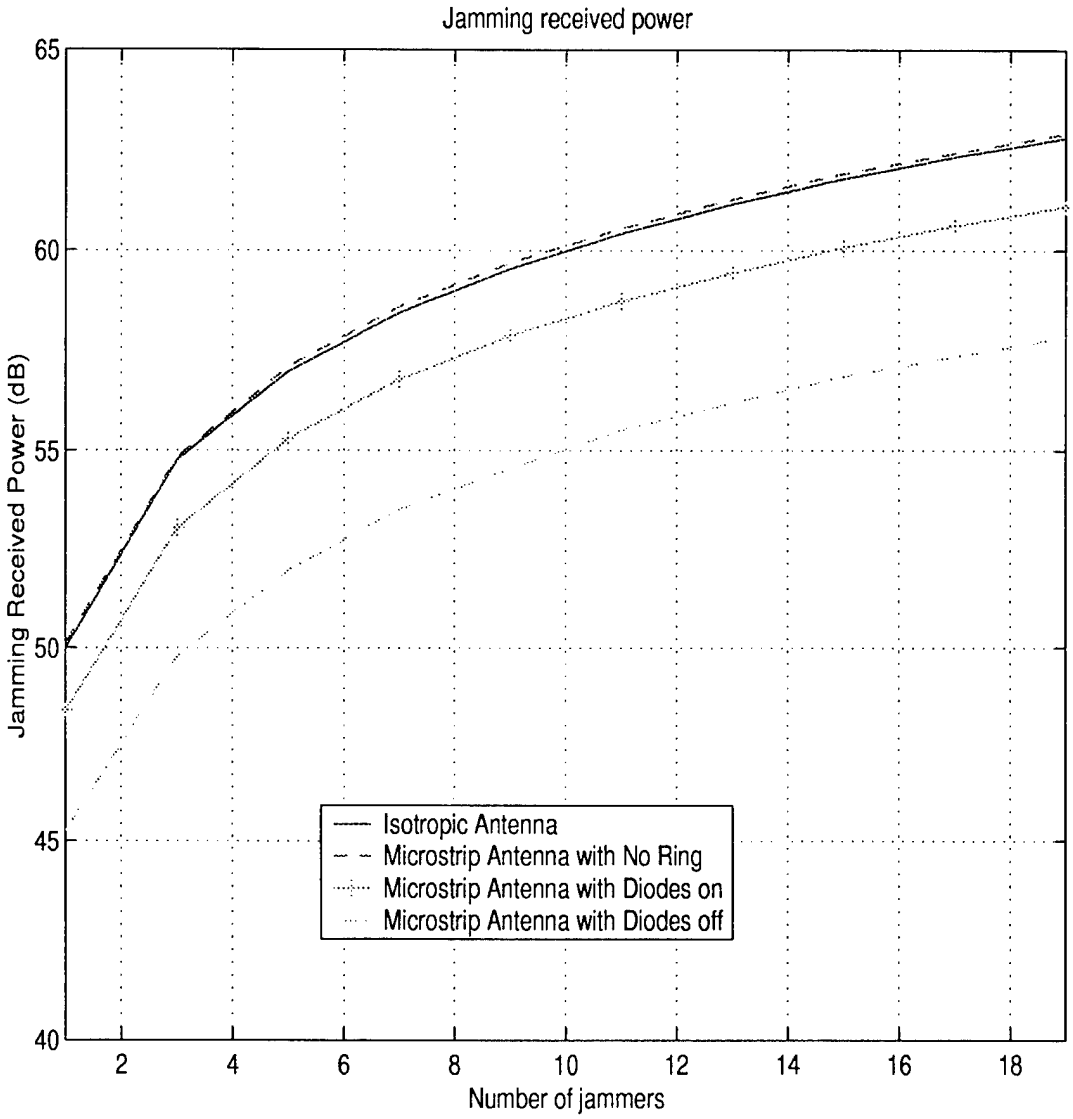

Figure 5.10: Received jamming power as a function of number of jammers

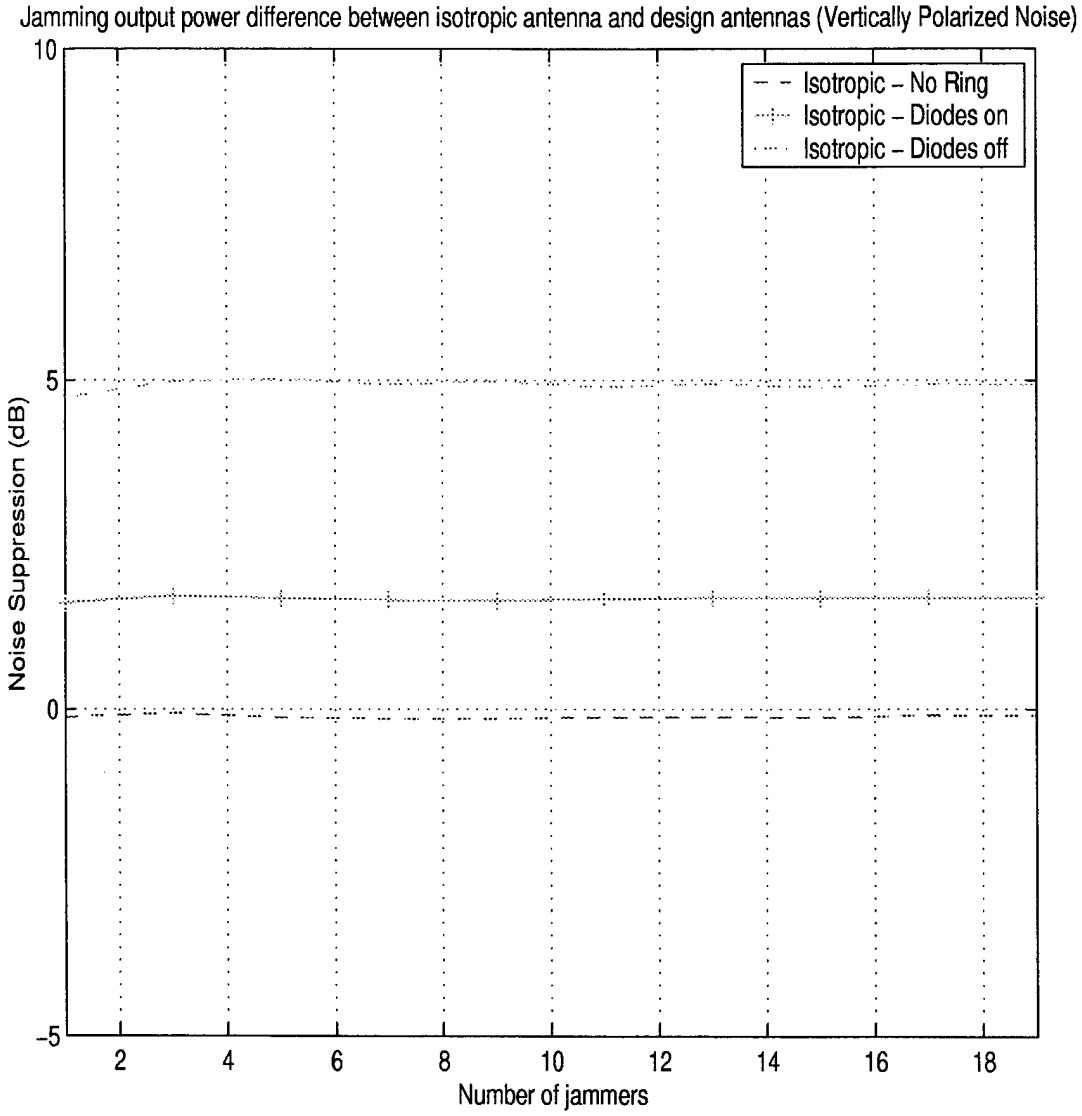

Figure 5.11: Interference suppression of the reconfigurable antenna with respect to ideal isotropic antenna

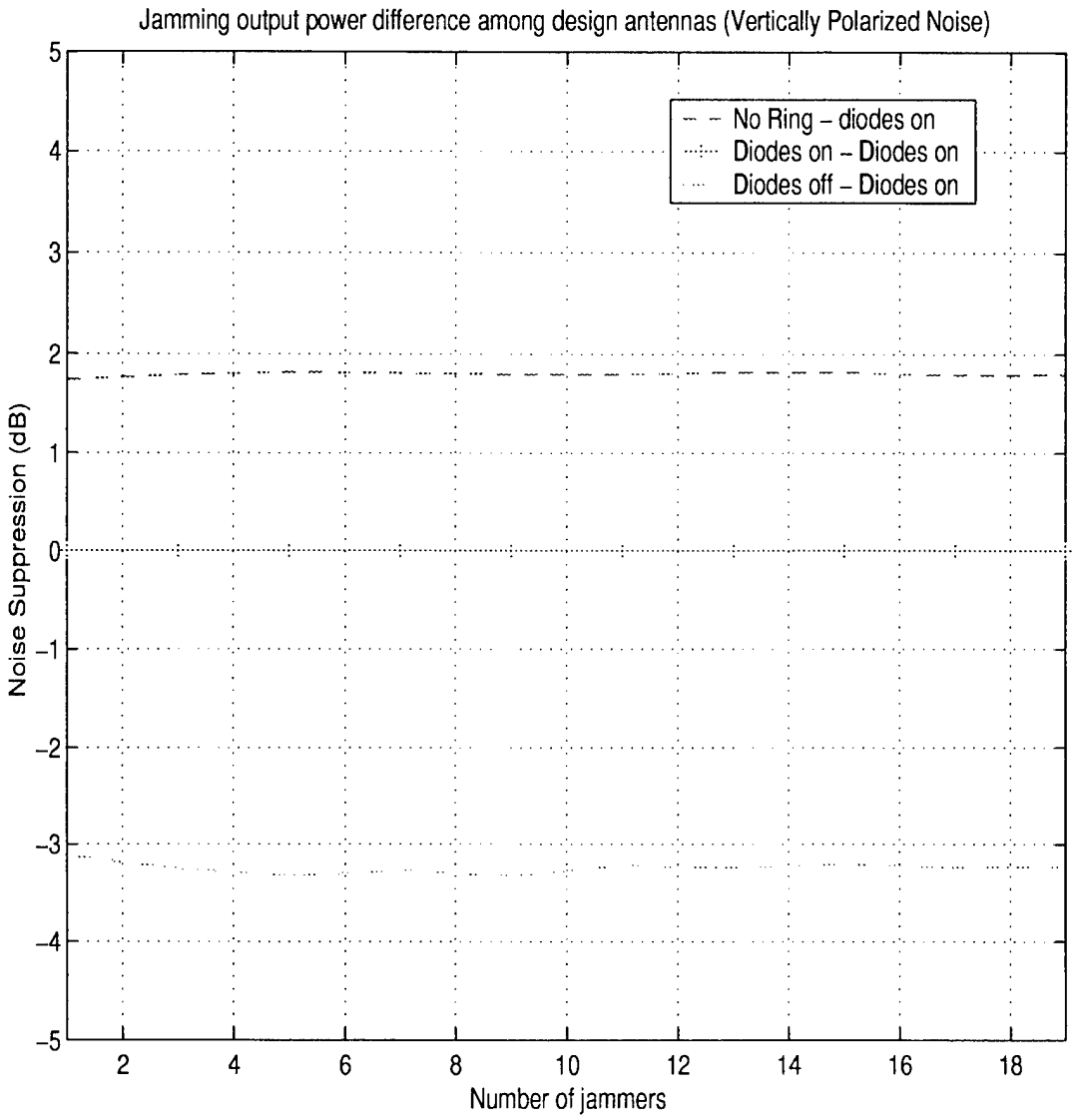

Figure 5.12: Interference suppression of reconfigurable antenna with respect to case when all switches in parasitic ring are turned on

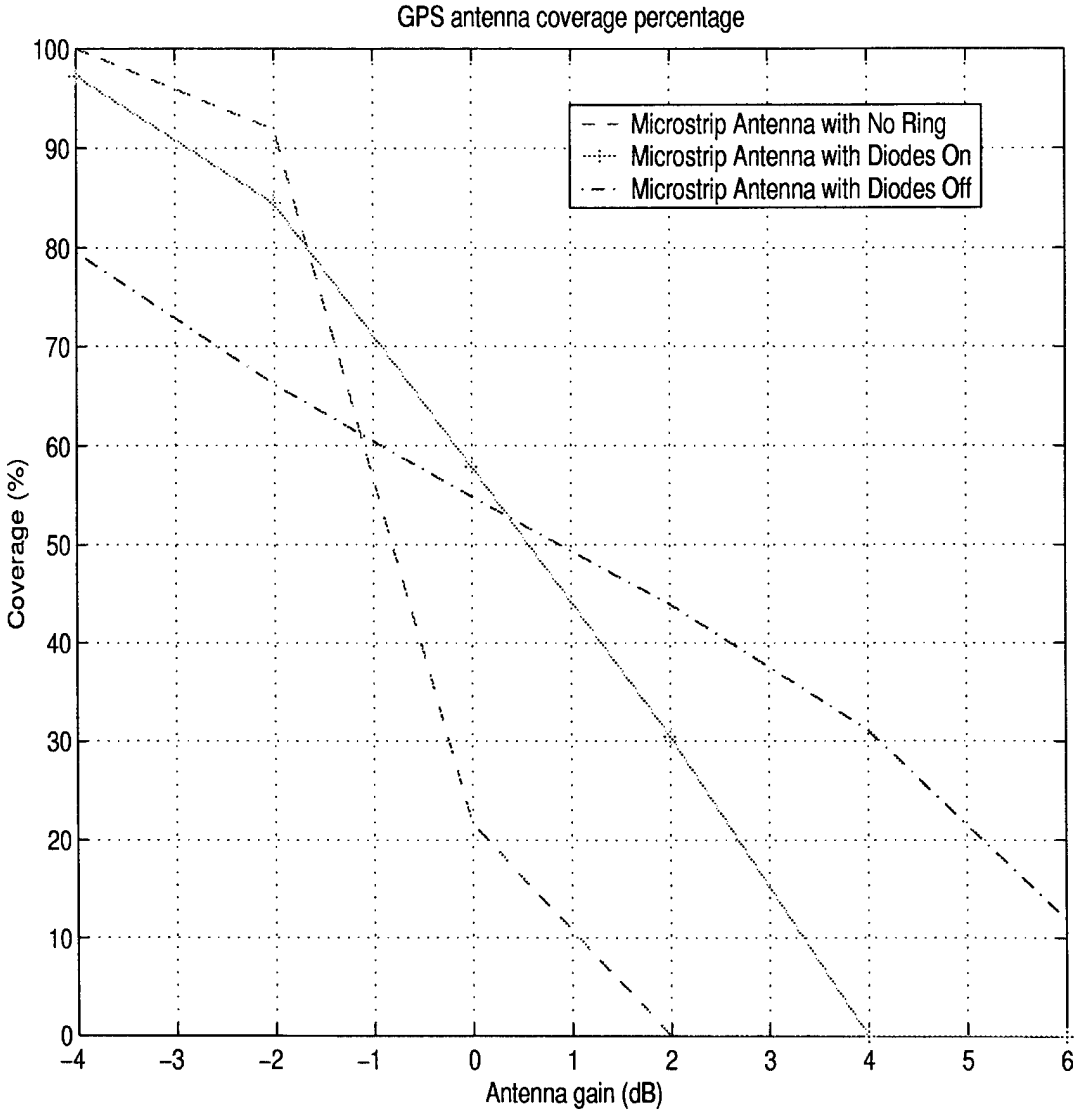

Figure 5.13: GPS antenna coverage as a function of antenna gain $\tilde{G}$

Chapter 6

Conclusion

In this report, we addressed three issues concerning the design and analysis of a reconfigurable printed antenna (Design II) for GPS applications. We conducted some parametric studies to determine the effect of some antenna dimensions on the far zone radiation pattern of a circularly polarized microstrip antenna. As demonstrated in the previous chapters, the ground plane size has to be carefully chosen to achieve a good antenna pattern. If the ground plane is too small, no field will be radiated from the patch. Likewise, the different parasitic ring dimensions yield different radiation patterns in terms of beamwidth and mainlobe level. The microstrip antenna with a larger ring dimension tends to have a RHCP radiation pattern with a larger beamwidth when the substrate thickness is around 0.8 cm (ϵ_r=9.2). On the other hand, when the substrate becomes thinner (around 0.27 cm), the beamwidth becomes larger as the ring becomes smaller. If the thickness becomes even smaller, the pattern does not change when the ring dimensions change because the surface waves excited within the substrate are very weak. The effect of the size of the ground plane was also considered. The ground plane has to be smaller than the ring (Design II) for the antenna to be reconfigurable. If the ground plane is larger, the pattern will not change when the switches are turn on and off. In addition, the different dielectric substrate dimensions don't play an important role when the substrate is much larger than the ring. This is expected since the edge effects from the substrate become weak when the substrate is large. When the substrate is about the same size as the ring, it can have a significant effect on the pattern.

We also briefly presented and scheme to reduce the overall size of the ring for Design II. It has been shown that inductive loading will reduce the size of the ring, while capacitive loading will have the opposite effect. A comparison between a Yagi-Uda array and a reconfigurable printed antennas was conducted. Both relay in parasitic elements to shape the radiation pattern. It was noted that the Yagi-Uda array uses free-space waves for the coupling, whereas, the reconfigurable array uses surface waves.

Besides the parametric studies, some improvements in the input impedance calculations are demonstrated in Chapter 4. Clearly, the calculations from the modified FDTD code match the real part of the measured results quite well. However, there is a mismatch between the modified FDTD and measured reactance. Although they have the same shape, the magnitudes are not the same. One reason is that the probe radius for the measured and calculated results might be different. We are still investigating the cause of this mismatch. Finally, the thin slot modification yields accurate field patterns when compared to patterns computed with an unmodified FDTD code. This modification will allow us to have a larger grid size, which will reduce the size of the computational domain and yield a more efficient design tool.

In chapter 5 we carried out simulations to assess the performance of a reconfigurable antenna (Design I) in the presence of jamming signals. Keeping in mind that the antenna will be mounted on the fuselage of an aircraft, we calculated the radiation patterns of the antenna mounted on an infinite planar ground plane. This ground plane models the fuselage which is assumed to be large in terms of wavelengths. In future work we will model the actual fuselage. Design I was used because it is assumed that the jamming signals are vertically polarized. If the signals were horizontally polarized, Design II would be have been used. As expected, there has to be a trade off between the performance in the presence of jamming signals and coverage. The narrower the beamwidth, the better the performance in the presence of jamming signals incident from directions around the horizon. However, the coverage deteriorates because the desired signals are coming from satellites.

In terms of future work, we will design and build a reconfigurable printed antenna. To accomplish this task, we first need to design a dual band (L1 and L2) circularly polarized printed antenna. We are currently working in that design. We will use diodes as the electrical switches. Another future task will be the simulation of the reconfigurable antenna when mounted on the fuselage of an aircraft. We are also working to improve the performance of Design II in the presence of vertically polarized jamming signals. Design II is more desirable because it is smaller in size than Design I.

Bibliography

[1] N. Padros, J. I. Ortigosa, M. F. Iskander, and B. Thornberg, "Comparative study of high-peformance gps receiving antenna designs," *IEEE Trans. Antennas Propagat.*, vol. 45, pp. 698–706, April 1997.

[2] I. J. Bahl and P. Bhartia, *Microstrip Antennas.* Massachusetts: Artech House, 1980.

[3] K. W. Lee and R. G. Rojas, "Study of novel adaptive printed antenna element using surface waves," *Dig. Int. Symp. Antennas Propagat. Soc.*, July 1999.

[4] K. W. Lee and R. G. Rojas, "Novel scheme for design of adaptive printed antenna elements," *2000 IEEE AP-S International Symposium and URSI Radio Science Meeting, Salt Lake City, Utah*, July 16-21 2000.

[5] R. G. Rojas and K. W. Lee, "Analysis and design of Novel Adaptive Printed Antennas for GPS Appplications," Tech. Rep. 737675-1, The Ohio State University ElectroScience Lab., December 1999.

[6] K. W. Lee and R. G. Rojas, "Reconfigurable GPS Antenna," Tech. Rep. 737675-2, The Ohio State University ElectroScience Lab., August 2000.

[7] W. F. Richards, *Microstrip Antennas*, ch. 10. NY: Van Nostrand Company, 1988.

[8] C. A. Balanis, *Advanced Engineering Electromagnetics.* NY: Wiley, 1989.

[9] P. S. H. J. R. James and C. Wood, *Microstrip Antenna Theory and Design.* P. Peregrinus Ltd., 1981.

[10] E. R. Brown, "Rf-mems switches for reconfigulable integrated circuits," *IEEE Trans. Microwave Theory Tech., Vol46, pp. 1868-1880*, Nov. 1998.

[11] R. G. Rojas and K. W. Lee, "Control of surface waves in planar printed antennas," *IEEE APS International Symposium and URSI Radio Science Meeting, Atlanta, Georgia, (invited paper)*, June 1998.

[12] R. G. Rojas and K. W. Lee, "Surface wave control in printed antennas using non-periodic parasitic strips," *to appear in IEE Proceeding Microwaves, Antennas and Propagat., Vol. 148*, February 2001.

[13] J. D. Kraus, *Antennas.* New York: Mcgraw-Hill, 1988.

[14] C. A. Balanis, *Antenna Thoery: Analysis and Design.* New York, 2nd ed.: Wiley, 1997.

[15] A. Taflove, *Computational Electrodynamics:The Finite-Difference Time-Domain method.* BOSTON: Artech House, 1995.

[16] E. Chang, S. A. Long, and W. F. Richards, "An experimental investigation of electically thick rectangular microstrip antennas," *IEEE Trans. Antennas Propagat.*, vol. 34, pp. 767–772, June 1986.

[17] A. Taflove, K. R. Umashankar, B. Beker, F. HarFoush, and K. Yee, "Detaied fd-td analysis of electromagnetic fields penetrating narrow slots and lapped joints in thick conducting screens," *IEEE Trans. Antennas Propagat.*, Febuary 1988.

[18] K.-L. Wong, W.-H. Hsu, and C.-K. Wu, "Single-feed circularly polarized microstrip antenna with a slit," *Microwave and Optical Technology Letters, Vol. 18, No. 4*, July 1998.

[19] R. Rojas and N. Surittikul, "Reconfigurable Printed Antenna for GPS Applications," Tech. Rep. 739356-1, The Ohio State University ElectroScience Lab., April 2001.